

Contents lists available at ScienceDirect

Petroleum Science

journal homepage: www.keaipublishing.com/en/journals/petroleum-science



Original Paper

Numerical simulation of vortex-induced vibration of deepwater drilling riser based on discrete vortex method



Yan-Bin Wang *, Hong-Chuan Zhao, De-Li Gao, Rui Li

MOE Key Laboratory of Petroleum Engineering in China University of Petroleum, Beijing, 102249, China

ARTICLE INFO

Article history: Received 16 October 2024 Received in revised form 11 March 2025 Accepted 11 March 2025 Available online 12 March 2025

Edited by Jia-Jia Fei

Keywords: Deepwater drilling riser Vortex-induced vibration Discrete vortex method Numerical simulation VIV suppression

ABSTRACT

Deepwater drilling riser is the key equipment connecting the subsea wellhead and floating drilling platform. Due to complex marine environment, vortex-induced vibration (VIV) will be generated on riser, which will induce fatigue failure and even cause unpredictable drilling accidents. Therefore, it is important to study the VIV characteristics of deepwater drilling riser and reveal the main controlling factors for ensuring the safe and efficient operation of deepwater drilling engineering. In this paper, the VIV of deepwater drilling riser is numerically simulated in time domain based on the discrete vortex method (DVM). A hydrodynamic analysis model and governing equation of VIV is proposed with considering the effect of riser motion using DVM and slice method, where the governing equation is solved by Runge-Kutta method. Model validation is performed, which verified the correctness and accuracy of the mechanical model and the solution method. On this basis, the influence of the number of control points, current velocity, riser outer diameter, shear flow and top tension on the VIV characteristics of deepwater drilling risers are discussed in detail. The results show that with the increase of current velocity, the vibration amplitude of deepwater drilling riser decreases obviously, while the vibration frequency increases gradually. However, if the outer diameter of riser increases, the vibration amplitude increases, while the vibration frequency decreases gradually. The top tension also has great influence on the VIV of riser. When the top tension is 1.25 G, the VIV is suppressed to a certain extent. This study has guiding significance for optimal design and engineering control of deepwater drilling riser. © 2025 The Authors. Publishing services by Elsevier B.V. on behalf of KeAi Communications Co. Ltd. This is an open access article under the CC BY license (http://creativecommons.org/licenses/by/4.0/).

1. Introduction

Deepwater drilling riser is only equipment connecting the subsea wellhead and floating platform in deepwater drilling engineering. However, due to complex marine environment, complex mechanical behavior will be generated on riser. Among them, vortex-induced vibration (VIV) is a common and complex mechanical behavior, which will lead to fatigue damage of riser. Therefore, it is important to study the VIV for the safe and efficient operation of riser.

Due to the importance and complexity of VIV, continuous and in-depth research has been carried out. Currently, the main research methods for VIV of deepwater drilling riser include physical experiments and numerical simulations. In the field of physical experiments, Feng (1968) has conducted VIV experiments in a wind tunnel and found that the frequency of vortex shedding is

nearly equal to the natural frequency of the cylinder when the VIV is in lock-in regions. Khalak and Williamson (1999) have measured the lift and drag coefficients as well as the amplitude response of cylinders and found that the vibration frequency of the cylinder is higher than its natural frequency when VIV lies in the lower branch. Oertel (1990) has demonstrated the presence of an unstable region in the wake flow, and pointed out that the unstable region is important to effectively control the VIV characteristics. Norberg (2003) has investigated the lift force on a cylinder subjected to crossflow and observed that the root mean square (RMS) of lift coefficient within a certain range of Reynolds number increases by approximately 10 times. In addition to experimental research, empirical methods and computational fluid dynamics (CFD) methods have been widely applied in study of VIV of deepwater flexible structures. The nonlinear wake oscillator is commonly used in these models to study the VIV of the structures (Birkhoff and Zarantanello, 1957; Bishop and Hassan, 1964; Hartlen and Currie, 1970; Facchinetti et al., 2004; Farshidianfar and Zanganeh, 2010). Kumar and Nallayarasu (2022) have investigated the VIV of long

E-mail address: wangyanbin@cup.edu.cn (Y.-B. Wang).

^{*} Corresponding author.

flexible riser under different aspect ratios, stiffness, mass ratios and axial force by using wake oscillator model, which found that 90% reduction in VIV displacement has been achieved by helical configurations. Besides, the influence of internal and external flow on VIV of deepsea mining riser has been studied (Mao et al., 2023), which indicated that the natural frequency of riser is negative correlation with internal flow while positively correlation with vibration amplitude. In addition, the influence of platform motion and unsteady flow on VIV have been evaluated, which showed that the VIV is significantly suppressed under the circumstance of the transition-low-frequency excitation parameters interacted with short-period unsteady flow (Li et al., 2023). However, the accuracy of the above empirical models is still limited by the choice of calculation parameters and the basic assumptions of the model. Furthermore, the flow field cannot be adequately described using these empirical methods. Thus, CFD methods are being used in more and more research. Direct numerical simulation (DNS) method has been used to investigated the VIV of long flexible risers under shear flow with Reynolds number of 1000, which shows that structural vibration manifests in the form of standing wave when shear flow is linearly distributed (Lucor and Karniadakis, 2001). Dynamic mesh technology is used to simulate the VIV characteristics under the condition of small mass ratio and damping effect through importing the cylinder vibration solver into user define function (UDF) compilation or compiled calculation program (Zhao et al., 2010; Li et al., 2021). In addition, VIV characteristics of long flexible risers both on inline direction and cross-flow direction have been studied with consideration the influence of shear flow (Bourguet et al., 2011). However, CFD methods are based on numerical implementation over millions of grids within the flow field, meaning a significant portion of the computational work is needed on the technical details related to grid generation which also requires considerable computational resources. Thus, meshless methods have rapidly developed to improve computational efficiency in recent years. Among them, DVM is an efficient meshless numerical method that simulates the flow field by discretizing the vorticity field into vortex elements. DVM has been demonstrated with several advantages such as fast computation speed, high flexibility, the ability to perform without high-quality grids and particularly suitable for simulating flow fields with complex boundaries and irregular flow. Thus, the DVM method has been widely used to calculate the vortex shedding frequencies, vortex patterns and force characteristics at certain Reynolds numbers (Chorin, 1973; Lewis, 1991; Owen et al., 1975; Griffin and Steven, 1976; Rimmer, 2001; Tian, 2016). In addition, three-dimensional numerical simulations of riser VIV have also been performed by using slice method under the circumstance of uniform and shear

However, the influence of riser motion is ignored in current VIV studies, which leads to considerable difference between the calculated results and the actual situation. Therefore, a numerical calculation model and method for VIV of deepwater drilling riser are proposed with consideration of the coupling effect of discrete vortex model and riser motion by using DVM, discrete vortex model and slice method in this paper. In the model, the slice method is used to perform hydrodynamic simulations at each node of the discrete riser. The riser VIV is then coupled with the discrete vortex model and the dynamic response equations of riser. Then, the governing equation is solved by Runge-Kutta method, and model validation is performed to illustrate the correctness of the model and method established in this paper. This research is of significance for a deeper understanding of VIV of deepwater drilling risers.

2. Basic theoretical method

2.1. Basic equations of fluid mechanics

Generally, the Navier-Stokes equations are used to describe the process of fluid motion. The equations include mass conservation equation and momentum conservation equation. The mass conservation equation can be written as:

$$\frac{\partial \rho}{\partial t} + \nabla \cdot (\rho \mathbf{U}) = 0 \tag{1}$$

where, ρ is density of fluid, kg/m³; \boldsymbol{U} is velocity of fluid, m/s; ∇ is divergence.

Considering the force on the fluid and the inertia of the fluid, the momentum conservation equation is:

$$\rho\left(\frac{\partial \boldsymbol{U}}{\partial t} + \boldsymbol{U} \cdot \nabla \boldsymbol{U}\right) = -\nabla \boldsymbol{P} + \mu \nabla^2 \boldsymbol{U} + \rho g \tag{2}$$

where, $\boldsymbol{U} \cdot \nabla \boldsymbol{U}$ is convective; $-\nabla \boldsymbol{P}$ is pressure gradient; $\mu \nabla^2 \boldsymbol{U}$ is viscosity; ρg is gravity.

2.2. Generation and shedding of vortices

In this study, the VIV of deepwater drilling riser is simulated by DVM. In the model, vortex and vorticity are important parameters describing fluid characteristics. Generally, the vortex is a vector field representing the strength and direction of fluid rotation. In two-dimensional condition, the vortex vector can be written as:

$$\boldsymbol{\omega} = \nabla \times \boldsymbol{U} \tag{3}$$

Vortex strength is measured by vorticity, which quantifies the degree of fluid rotation. Compared with vortex, vorticity is more intuitive representation of vortex strength. For deepwater drilling riser, the flow field of cross section at a certain depth when current flows through the riser is shown in Fig. 1.

As shown in Fig. 1, the riser acts as an obstacle to the current resulting in increasing of local velocity and pressure and generating clockwise pressure gradient before current reaches point 2. After point 2, the obstructing effect gradually decreases, which results in

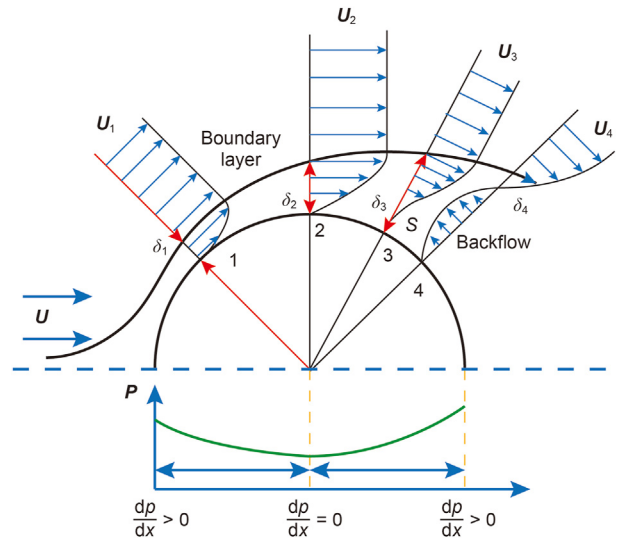


Fig. 1. Schematic diagram of boundary layer separation on riser surface.

reduction of local velocity, increase of pressure, and generating a reverse pressure gradient. The flow velocity near the riser wall gradually decreases with the increase of pressure gradient. After the flow velocity decreases to 0, a local backflow called vortex is formed. The vortex continues to form and shed at the back edge of riser as the flow continues. At present, the observation of vortex shedding mode of cylindrical wake is mainly realized by digital particle image velocimetry (DPIV) and CFD simulations. At present, six different vortex shedding modes, including SS, 2S, 2P, P + S, 2C and 2T, have been identified (Williamson and Roshko, 1988; Januvtis and Williamson, 2003). Among them, SS mode means two symmetric vortices are released during each vibration period, 2S mode means two vortices are released, 2P mode means two pairs of vortices with opposite rotation directions are released, P + S mode means a pair of vortices on one side and a vortex on the other side is released, 2C mode means two pairs of vortices with the same rotation direction are released, and the 2T mode means two groups of three vortices are released.

2.3. Strouhal number and vortex shedding frequency

Strouhal number (*St*) is one of the important dimensionless parameters to describe the vibration frequency and is usually used to characterize the ratio relationship between structural vibration frequency and fluid characteristic scale. It is also used to describe the degree of interaction between the vortex structure generated in the fluid and the structural vibration, which can be expressed as:

$$St = \frac{fL}{U} \tag{4}$$

where, f is vibration frequency of the structure, Hz; L is characteristic scale of fluid.

Vortex shedding frequency is usually depended on the Strouhal number, the geometry of the structure and the velocity of the fluid. However, when the vibration frequency of the structure is close to the vortex shedding frequency, resonance phenomenon may occur, which will result in increase of vibration amplitude. Therefore, the resonance phenomenon can be eased through adjusting the Strouhal number and controlling the interaction between the structure vibration and the fluid vortex.

2.4. Discrete vortex method

The DVM is a numerical method that can be used to describe and track the vortex structure in fluid mechanics. Different from traditional analysis methods, DVM does not directly simulate the fluid velocity field and pressure field, but decomposes the fluid domain into discrete vortex elements. The generation, evolution and the interaction of vortices are revealed by simulating the motion of vortex elements. Since the density of incompressible fluid is constant, Eq. (1) can be simplified as:

$$\nabla \cdot \boldsymbol{U} = 0 \tag{5}$$

If parameter φ is used to represent the velocity component with a velocity potential function, one obtains:

$$\mathbf{U} = \nabla \varphi \tag{6}$$

Substituting Eq. (6) into Eq. (5), the Laplace equation can be obtained:

$$\nabla^2 \varphi = 0 \tag{7}$$

Eq. (7) is a second-order partial differential equation, which can be solved to obtain the velocity of the vortex element at each point. The specific solution process of Eq. (7) is shown in Appendix A.

3. Numerical simulation of two-dimensional VIV using DVM

3.1. Vortex strength

The DVM is a numerical method used to simulate flow in fluid mechanics. Its basic idea is to represent the vortex structure in fluid flow as a series of discrete vortex elements, and to describe the characteristics of flow field by combining the strength and position of these vortex elements.

As shown in Fig. 2, the surface of riser is divided into N equal parts, and N panels are generated, where the midpoint of each panel is used as the control point in DVM. Generally, the cosine function is used to determine the horizontal and vertical coordinates of the starting point and the ending point of each panel, which are:

$$\chi = \frac{1 + \cos\beta}{2} \tag{8}$$

$$y = \frac{\sin\beta}{2} \tag{9}$$

where, β is the polar angle which ranges from 0 to 2π .

Thus, the end coordinates of each panel, the unit tangent vector, the unit normal vector and the coordinates of each control point can be figured out through Eqs. (8) and (9).

The vortex intensity of each vortex plane element can be calculated by:

$$\gamma = \left(K^{t}\right)^{-1} \cdot RHS \tag{10}$$

where, K is the influence coefficient matrix; $RHS_i = -(\boldsymbol{v}_{\infty X} \cdot \boldsymbol{t}_{ix} + \boldsymbol{v}_{\infty y} \cdot \boldsymbol{t}_{iy}); \boldsymbol{v}_{\infty} = (\boldsymbol{v}_{\infty X}, \boldsymbol{v}_{\infty y})$ is the inflow velocity; $\hat{\boldsymbol{t}}_i = (\boldsymbol{t}_{ix}, \boldsymbol{t}_{iy})$ is the unit tangent vector of the vortex element i. Refer to Appendix B for the derivation of Eq. (10).

3.2. Shedding of the vortex elements

In DVM, free vortex elements are continuously released into surrounding flow field from riser surface, and flow together with other vortex elements to form a wake field. Each panel will release one vortex element and the vortex element strength is equal to the vortex strength of its corresponding vortex plane element. Since the free vortex element in the wake field will also affect the calculation of the strength of each panel on riser surface, the free vortex element is necessary to be considered, the sum of the vorticity generated by free vortex elements at each vortex plane

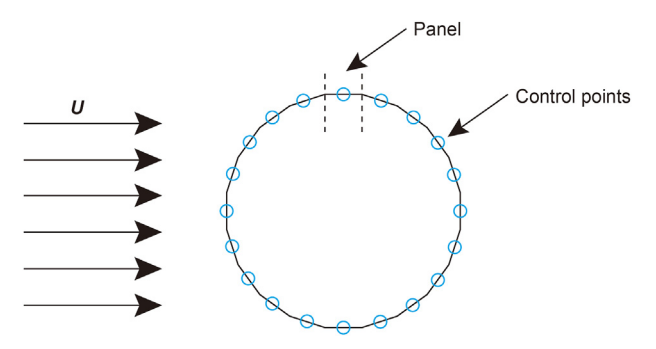


Fig. 2. Schematic diagram of boundary discretization.

element should be zero, which is:

$$\sum_{i=1}^{N} \mathbf{v}_{ik} \Delta S_i = 0 \tag{11}$$

Considering the influence of free vortex elements, one obtains:

$$\sum_{j=1}^{N} \left(K_{ij}^{t} + \Delta S_{j} \right) \cdot \gamma_{j} = - \left(\boldsymbol{v}_{\infty X} \cdot \boldsymbol{t}_{iX} + \boldsymbol{v}_{\infty y} \cdot \boldsymbol{t}_{iy} \right)$$

$$- \sum_{k=1}^{N_{v}} \Delta \Gamma_{k} \left(\widetilde{\boldsymbol{u}_{ik}} \cdot \boldsymbol{t}_{iX} + \widetilde{\boldsymbol{v}_{ik}} \cdot \boldsymbol{t}_{iy} \right)$$

$$(12)$$

where, $\widetilde{u_{ik}}$ and $\widetilde{v_{ik}}$ are induced velocity of a free vortex element in the x and y directions at a certain panel; $\Delta\Gamma_k$ is the strength of free vortex element and N_v is the total number of free vortex elements in the wake area.

Refer to Appendix C for the derivation of Eq. (12).

3.3. Convection of vortex elements

Generally, there are three main influencing factors should be considered for the convection process of discrete vortices. The first one is the free flow velocity which affects the overall motion and trajectory of the discrete vortices. The secondly one is the vorticity distribution on the panel which affects the velocity and behavior of the discrete vortices. The third one is the influence of other vortices. In order to accurately simulate the convection process, the above three factors must be considered simultaneously.

The velocity of a free vortex element in the *x* and *y* directions can be represented by:

$$u_{k} = \mathbf{v}_{\infty x} + \sum_{i=1}^{N} \gamma_{i} \widetilde{u_{ki}^{p}} + \sum_{i=1}^{N_{y}} \Delta \Gamma_{i} \widetilde{u_{kj}}$$

$$j \neq k$$
(13)

$$v_{k} = \mathbf{v}_{\infty x} + \sum_{i=1}^{N} \gamma_{i} \widetilde{v_{ki}^{p}} + \sum_{i=1}^{N_{v}} \Delta \Gamma_{i} \widetilde{\mathbf{v}_{kj}}$$

$$i \neq k$$
(14)

where, $\mathbf{v}_{\infty \mathbf{v}}$ and $\mathbf{v}_{\infty \mathbf{y}}$ are influence terms of the free inflow; $\sum_{i=1}^{N} \gamma_{i} \widetilde{u}_{ki}^{p}$ and $\sum_{i=1}^{N} \gamma_{i} \widetilde{v}_{ki}^{p}$ are influence terms of the panels; $\sum_{i=1}^{N_{v}} \Delta \Gamma_{i} \widetilde{u}_{kj}$ and $\sum_{i=1}^{N_{v}} \Delta \Gamma_{i} \widetilde{v}_{kj}$ are influence terms of free vortex

$$j \neq k$$
 $j \neq k$

elements

When the velocity of the free vortex elements at a certain time step are obtained, the position of the free vortex elements can be figured out, which are:

$$\mathbf{x}_{k}^{'} = \mathbf{x}_{k} + \mathbf{u}_{k} \cdot \Delta t \tag{15}$$

$$y_{\nu}^{'} = y_{k} + \mathbf{v}_{k} \cdot \Delta t \tag{16}$$

where, x_k' and y_k' are new position components of a certain free vortex element in x and y directions. However, the above calculation model regards the motion trajectory of free vortex elements in a time step as a straight line while the actual motion trajectory should be a curve, which will lead to calculation error. As the calculation time continues, the calculation error accumulates,

which is also known as numerical viscous error. In order to reduce this error, the modified Euler method is used to calculate the motion path of the free vortex element. In this case, the position of a certain free vortex element can be calculated by:

$$x_{k}^{'} = x_{k} + \frac{\mathbf{u}_{k}^{1} + \mathbf{u}_{k}^{2}}{2} \cdot \Delta t \tag{17}$$

$$y_k' = y_k + \frac{\mathbf{v}_k^1 + \mathbf{v}_k^2}{2} \cdot \Delta t \tag{18}$$

where, \boldsymbol{u}_k^1 and \boldsymbol{v}_k^1 are the velocity of a certain vortex element after the first convection; \boldsymbol{u}_k^2 and \boldsymbol{v}_k^2 are the velocity of a certain vortex element after the second convection.

Table 1Simulation parameters.

Parameter	Value	Parameter	Value
Inflow velocity, m/s	1	Cylinder diameter, m	1
Reynolds number	10 ⁵	Time step, s	0.0245
Number of the discretization	64	Total time, s	50

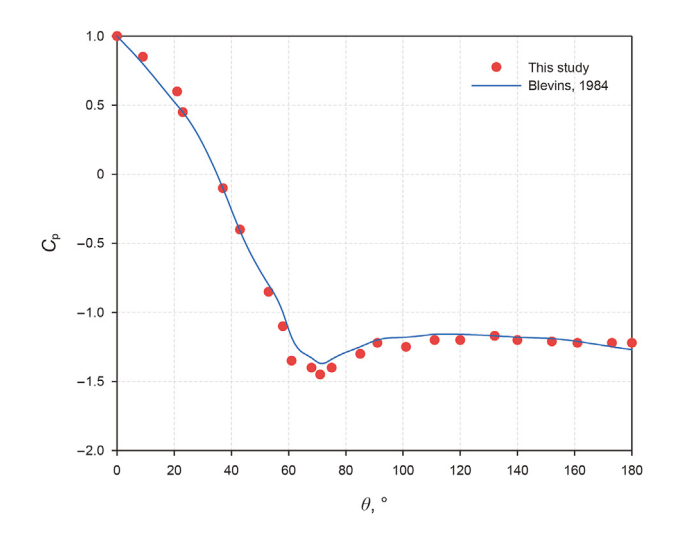


Fig. 3. Riser surface pressure coefficient.

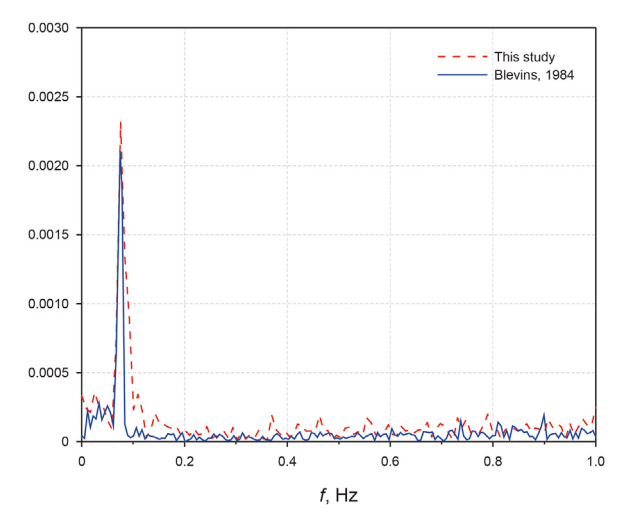


Fig. 4. Lift coefficient power spectrum.

3.4. Diffusion of vortex elements

For the viscous diffusion term in DVM, a random method is proposed to simulate the evolution of the whole discrete vortex system by introducing some randomness in each time step (Chorin,

1973). If the Reynolds number is relatively high, the diffusion term has little influence on the flow field, otherwise the diffusion term is dominant. Under this circumstance, the two-dimensional Navier-Stokes equation can be represented by:

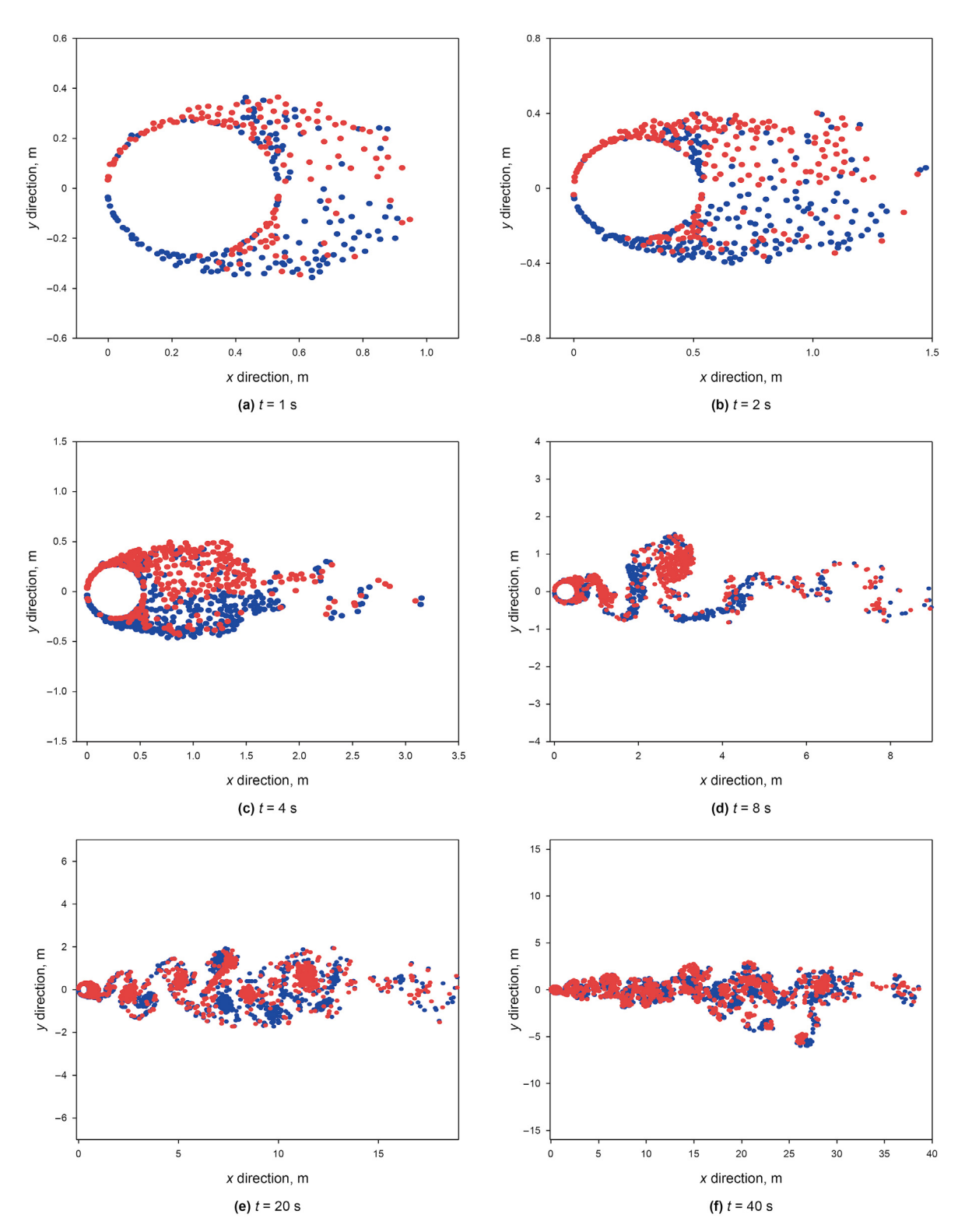


Fig. 5. Shapes of vortices behind riser at different time.

Table 2 Numerical simulation parameters.

Parameter	Value	Parameter	Value
Inflow velocity, m/s	$ \begin{array}{c} 1 \\ 5.3 \times 10^5 \\ 0.0245 \end{array} $	Riser outer diameter, mm	533.4
Reynolds number		End time, s	40
Time step, s		Number of control points	30

The simulation results are shown in Fig. 5.

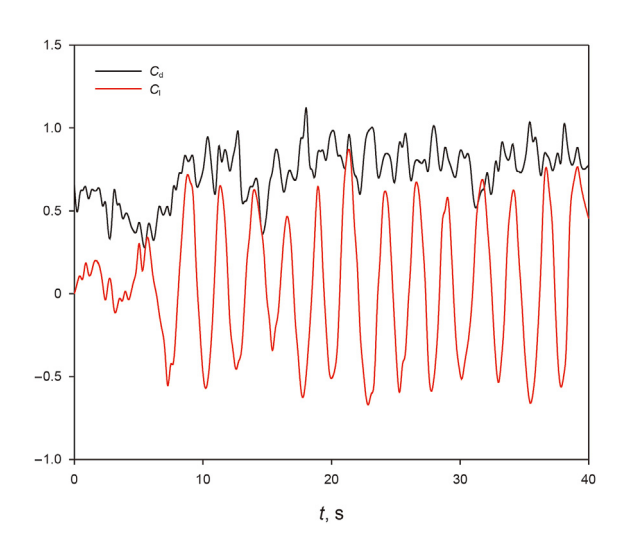


Fig. 6. Time history curve of the riser lift coefficient and resistance coefficient.

$$\frac{\partial \omega}{\partial t} = \mu \nabla^2 \omega \tag{19}$$

In polar coordinates, Eq. (19) can be written as:

$$\frac{\partial \omega}{\partial t} = \mu \left(\frac{\partial^2 \omega}{\partial r^2} + \frac{1}{r} \frac{\partial \omega}{\partial r} \right) \tag{20}$$

The basic solution of Eq. (20) is:

$$\omega(r,t) = \frac{\Gamma}{4\pi\mu t} e^{\left(-\frac{r^2}{4\mu t}\right)} \tag{21}$$

The random displacement of each free vortex element in each time step is:

$$\Delta x_k = \left(4\mu\Delta t \ln\frac{1}{P_k}\right)^{1/2} \cos\Delta\theta_k \tag{22}$$

$$\Delta y_k = \left(4\mu\Delta t \ln\frac{1}{P_k}\right)^{1/2} \sin\Delta\theta_k \tag{23}$$

where, P_k and $\Delta\theta_k$ are random variables, which ranges from 0 to 1 and 0 to 2π , respectively.

When the free vortex element completes convection and diffusion, the lift coefficient and drag coefficient of the riser can be obtained, which are:

$$C_{\rm l} = CF_{\rm v} \cos \alpha - CF_{\rm x} \sin \alpha \tag{26}$$

$$C_{\rm d} = CF_{\rm y} \sin\alpha - CF_{\rm x} \cos\alpha \tag{27}$$

where, α is the angle between the vortex plane and the horizontal direction.

Refer to Appendix D for the derivation of Eqs. (26) and (27).

3.5. Influence of the riser motion

In this paper, the riser motion is considered in the VIV analysis, which is simulated by adding the motion velocity term to the boundary conditions. If the riser velocity at certain time t is $\mathbf{v}_{\rm b}$ and the $j^{\rm th}$ vortex element is acting on the riser, the velocity at vortex element i consists of three parts including the inflow velocity, the induced velocity of all vortex elements and the velocity of the object, which is:

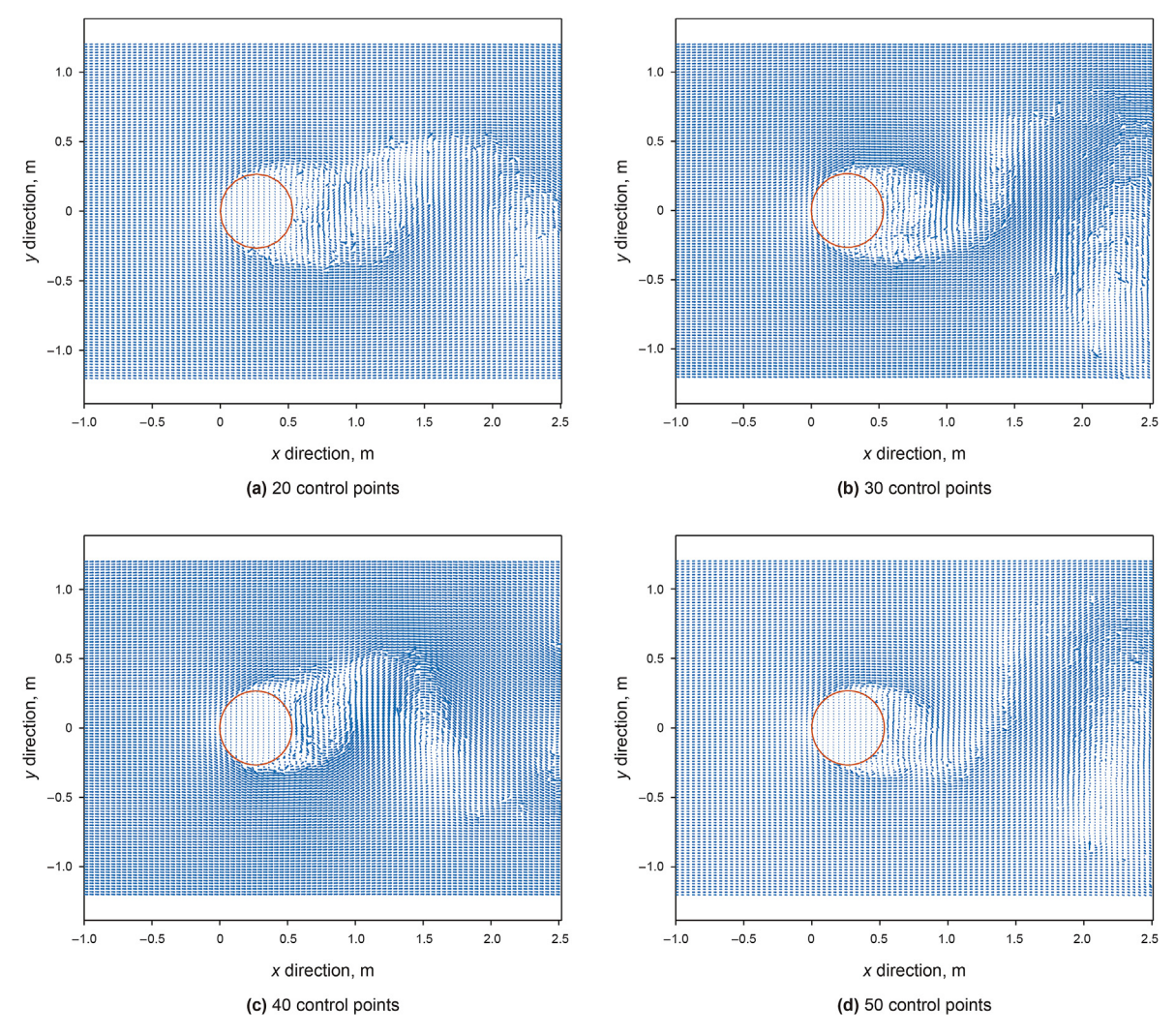


Fig. 8. Velocity field distribution under different control points.

$$\mathbf{v}_i = \mathbf{v}_{\infty} + \sum_{i=1}^{N} \mathbf{v}_{ij}^p + \mathbf{v}_{b}$$
 (28)

where, $v_{\rm b}$ is the velocity of riser.

Considering the Dirichlet condition on the boundary conditions, one obtains:

$$\boldsymbol{v}_{\infty} \cdot \hat{\boldsymbol{t}}_{i} + \sum_{i=1}^{N} \boldsymbol{v}_{ij}^{p} \cdot \hat{\boldsymbol{t}}_{i} + \boldsymbol{v}_{b} \cdot \hat{\boldsymbol{t}}_{i} = 0$$
(29)

In the case of riser motion, Eq. (11) can be written as:

$$\sum_{j=1}^{N} K_{ij}^{t} \cdot \gamma_{j} = -(\boldsymbol{v}_{\infty x} \cdot \boldsymbol{t}_{ix} + \boldsymbol{v}_{\infty y} \cdot \boldsymbol{t}_{iy}) - (\boldsymbol{v}_{bx} \cdot \boldsymbol{t}_{ix} + \boldsymbol{v}_{by} \cdot \boldsymbol{t}_{iy})$$
$$- \sum_{k=1}^{N_{v}} \Delta \Gamma_{k} (\widetilde{u_{ik}} \cdot \boldsymbol{t}_{ix} + \widetilde{v_{ik}} \cdot \boldsymbol{t}_{iy})$$
(30)

By comparing Eq. (11) and Eq. (30), the coefficient matrix in Eq. (11) is the same as that in Eq. (30).

4. Numerical simulation

4.1. Simulation results and discussion without considering riser motion

4.1.1. Model validation

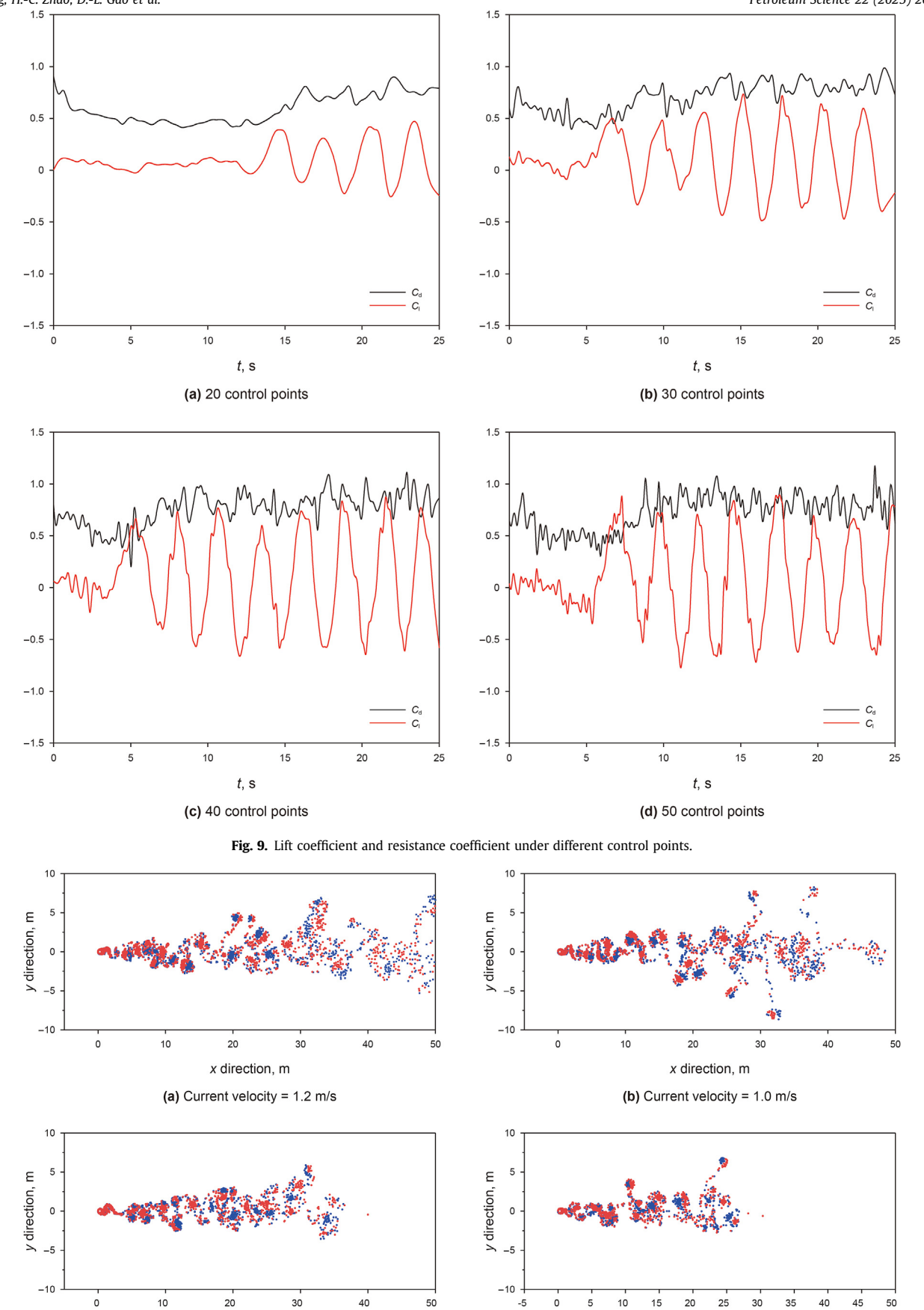
The analysis results obtained in this paper is compared with the results of previous studies according to the data shown in Table 1 (Blevins, 1984). The calculation results of riser surface pressure coefficient and lift coefficient power spectrum are shown in Figs. 3 and 4, respectively.

As shown in Figs. 3 and 4, the results of the pressure coefficient in this paper are in good agreement with the experimental results, which proves the correctness of the model and the solution method in this paper.

4.1.2. Case study

After model validation, the process of vortex generation and shedding under certain inflow velocity is simulated. The simulation parameters are shown in Table 2.

As shown in Fig. 5(a) and (b), continuous vortices are generated from the control points at the beginning of numerical simulation. In particular, clockwise rotating vortices with blue color are generated at the control points on the upper edge of the riser, while



 $\textbf{Fig. 10.} \ \, \textbf{Shapes of vortices behind riser under different inflow velocity.} \\ 2049$

x direction, m

(d) Current velocity = 0.6 m/s

x direction, m

(c) Current velocity = 0.8 m/s

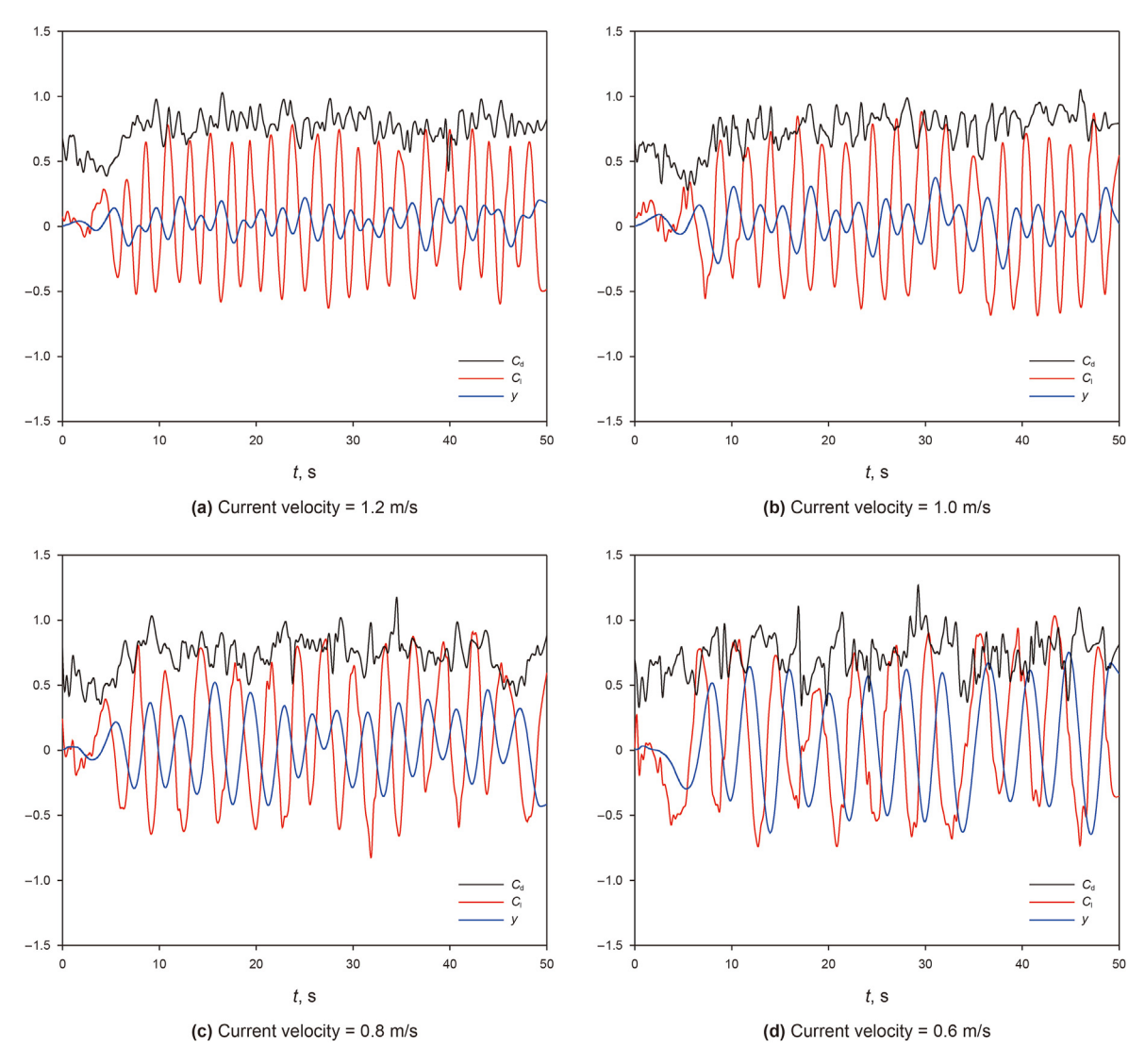


Fig. 11. Lift coefficient, resistance coefficient and dimensionless displacement of riser under different inflow velocity.

counterclockwise rotating vortices with red color are generated at the control points on the lower edge of the riser. As time going on, the generated vortex continuously accumulates behind the riser. As shown in Fig. 5(c), with the continuous generation of new vortices at the control points, the vortices gradually increase, which induces two large vortices with opposite rotation. As shown in Fig. 5(d), these vortices begin to shear and entrain each other and move slowly along the direction of the inflow, eventually shed from the boundary layer. As shown in Fig. 5(e) and (f), with the further increase of simulation time, more vortices shed from the riser and eventually form a periodic wake flow.

The calculated drag coefficient C_d and lift coefficient C_l is shown in Fig. 6.

As shown in Fig. 6, the drag coefficient C_d and lift coefficient C_l begin to show periodic fluctuations when t=8 s, which indicates that the vortex begins to shed from the riser taking the form of periods. After the vortex shedding is stable, the average value of C_d is 0.82 and the lift coefficient C_l fluctuates around 0.

4.1.3. Parameter sensitivity analysis

(1) Control points

The number of control points has a great influence on the simulation results. If the number of control points is excessive, the calculation cost will increase rapidly, while too few control points mean unpredictable error of simulation results. When the control points are 20, 30, 40 and 50, the simulated wake field, velocity field, lift coefficient and resistance coefficient are shown in Figs. 7–9.

As shown in Fig. 7, the vortex shedding mode alternates between 2S mode and 2P mode. In particular, the 2S mode appears near the trailing edge of the riser, which means two vortices with opposite rotating direction shed off in one period. The vortex shedding mode begins to change from 2S mode to 2P mode at 8 m away from the riser, which means two pairs of vortices fall off in each cycle and each pair consisting of two vortices with opposite rotating direction.

Fig. 8 shows the velocity vector distribution near the riser under different control points.

As shown in Fig. 8, the inflow is attached to the surface of the riser when the central angle of the riser is less than 120°. When the central angle of the riser is greater than 120°, the flow begins to separate from the surface of the riser.

Fig. 9 shows the change of the lift and resistance coefficients of the riser with time under different control points.

As shown in Fig. 9, when the number of control point is 20, the

vortex shedding starts at 13 s and there are 4 shedding periods within 25 s. When the number of control point is 30, 40 and 50, the vortex shedding starts at 7 s and there are 7 shedding periods within 25 s. In addition, with the increase of control points, the variation amplitude of lift coefficient also increases. After vortex shedding is stable, the drag coefficient is around 0.75. Under the above different control points, the total calculation time of the simulation is 30, 40, 110 and 230 min, respectively. It can be seen from the power spectrum of lift coefficient that the vortex shedding frequencies of the last three simulations are close to each other. Therefore, for risers of this geometric size, 30 control points meet the requirements of simulation accuracy.

(2) Current velocity

The simulated wake field, lift coefficient, drag coefficient and dimensionless displacement are shown in Figs. 10 and 11 when the inflow velocity is 1.2, 1.0, 0.8, and 0.6 m/s, respectively. The average

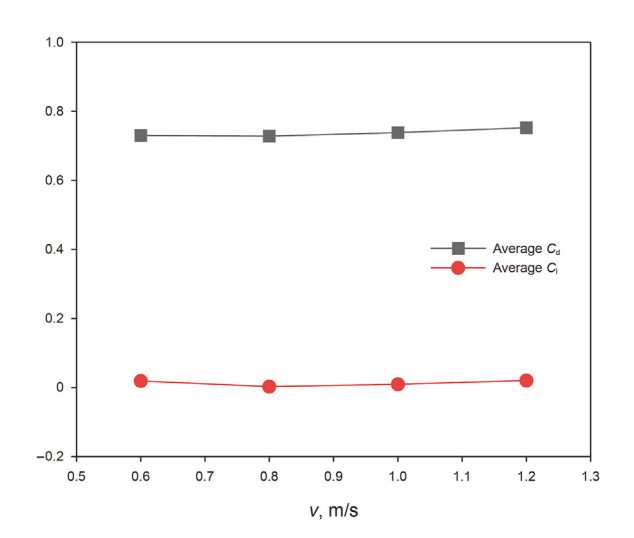


Fig. 12. Lift coefficient and resistance coefficient of the riser under different inflow velocity.

lift coefficient and drag coefficient are shown in Fig. 12.

Fig. 10 shows the distribution of vortices behind the riser at different inflow velocity. As shown in Fig. 10, 2S mode appears near the rear edge of the riser when the inflow velocity is 1.2 and 1.0 m/s. The shedding mode begins to change from 2S mode to 2P mode at 8 m away from the riser. With the decrease of the inflow velocity, the starting point of the 2P mode gradually moves forward. When the inflow velocity is 0.6 m/s, the 2S mode can no longer be observed.

Fig. 11 shows the simulation results of lift coefficient, resistance coefficient and dimensionless displacement of riser with time under different inflow velocity.

As shown in Fig. 11, with the continuous decrease of inflow velocity, the variation amplitude of lift coefficient increases, while the variation frequency gradually decreases, that is, the vortex shedding frequency gradually decreases. Besides, the amplitude of the dimensionless displacement of the riser vibration increases and the frequency decreases gradually. Moreover, the variation amplitude of resistance coefficient increases gradually.

Fig. 12 shows the variation of the average lift coefficient and drag coefficient under different inflow velocity.

As shown in Fig. 12, the average of lift coefficient always remains near 0 and the average drag coefficient increases slightly with the increase of inflow velocity. In addition, according to Figs. 10–12, with increasing inflow velocity, the onset of the 2P vortex-induced vibration mode shifts toward the trailing edge of the riser, while the operational range of the 2S mode contracts concurrently with a reduction in riser vibration amplitude. However, the influence of inflow velocity on the average resistance coefficient of riser is relatively small on the whole.

(3) Riser outer diameter

The simulated wake field, lift coefficient, resistance coefficient and dimensionless displacement are shown in Figs. 13 and 14 when the riser outer diameter is 0.25, 0.5, 0.75 and 1 m, respectively. The average value of lift coefficient and resistance coefficient is shown in Fig. 15.

Fig. 13 shows the distribution of vortex elements behind riser

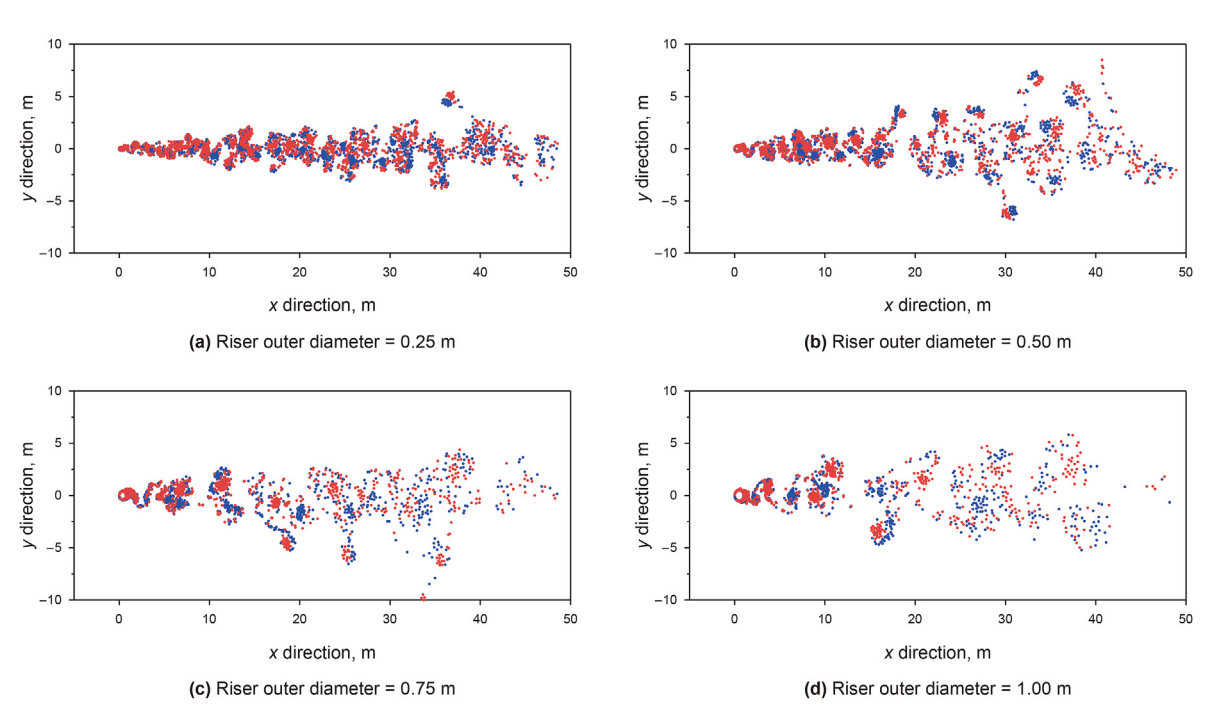


Fig. 13. Vortices distribution behind riser under different riser outer diameter.

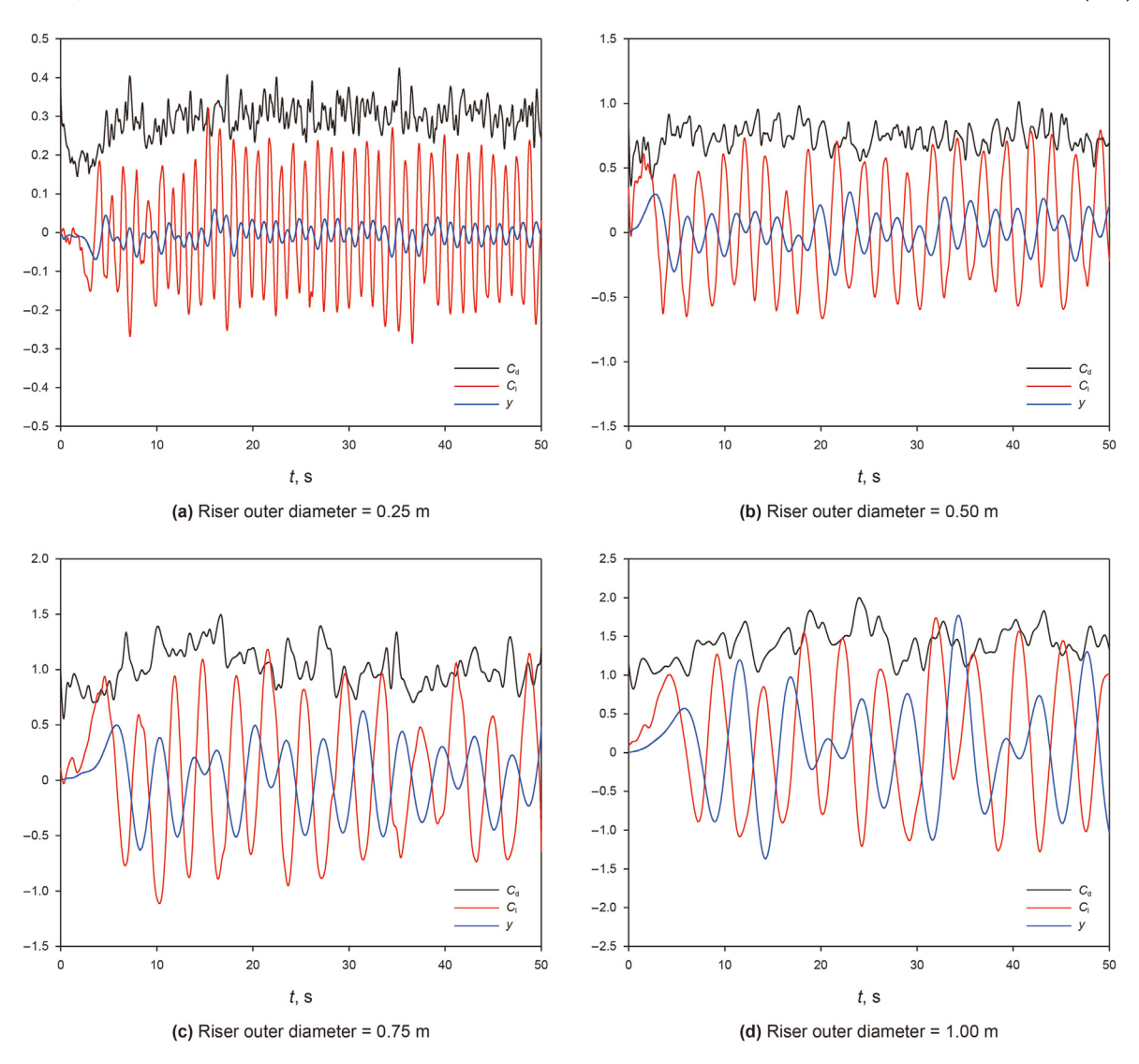


Fig. 14. Lift coefficient, resistance coefficient and dimensionless displacement of riser under different riser outer diameter.

under different riser outer diameter. As shown in Fig. 13, when riser outer diameter is 0.25 and 0.5 m, 2P mode near the trailing edge of riser is observed. However, when the riser diameter is 0.75 and 1.0 m, the 2P mode can be observed within 20 m behind the riser.

Fig. 14 shows the change of lift, resistance coefficient and dimensionless displacement of riser with time under different riser outer diameter. As shown in Fig. 14, with the increase of outer diameter, the variation amplitude of the lift coefficient increases, while the variation frequency decreases gradually. That is to say, the vortex shedding frequency behind the riser decreases gradually. The amplitude of the dimensionless displacement increases and the frequency decreases gradually. In addition, the variation amplitude of resistance coefficient increases gradually.

Fig. 15 show the average lift and drag coefficient under different riser outer diameter.

As shown in Fig. 15, the average lift coefficient is close to 0 and the average drag coefficient increases significantly with the increase of incoming flow velocity, which indicates that the fluid resistance on the riser increases substantially. As can be seen from Figs. 13—15, the riser out diameter has great influence on the average resistance coefficient of the riser. In particular, the range of

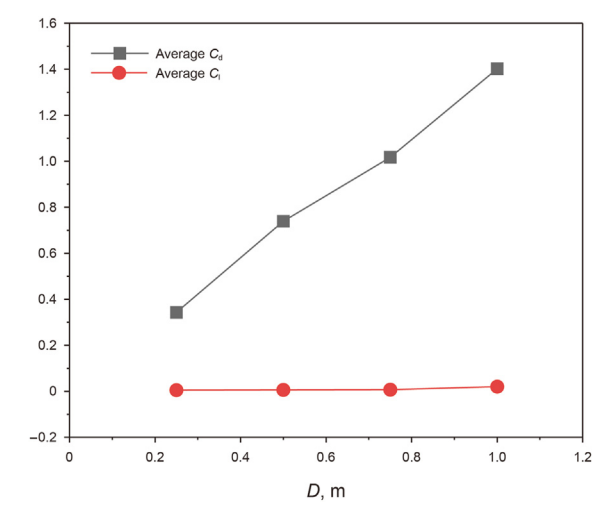


Fig. 15. Lift coefficient and resistance coefficient of riser under different riser outer diameter.

Table 3 Simulation parameters.

Parameter	Value	Parameter	Value
Water depth, m	3012	Outer diameter in bare regions, m	0.6
Flexural rigidity, kN·m ²	316051	Outer diameter in buoyant regions, m	1
Current velocity (at sea surface), m/s	1.2	Current velocity (at seabed), m/s	0.4
Top tension, kN	1699	Steel density, kg/m ³	7850

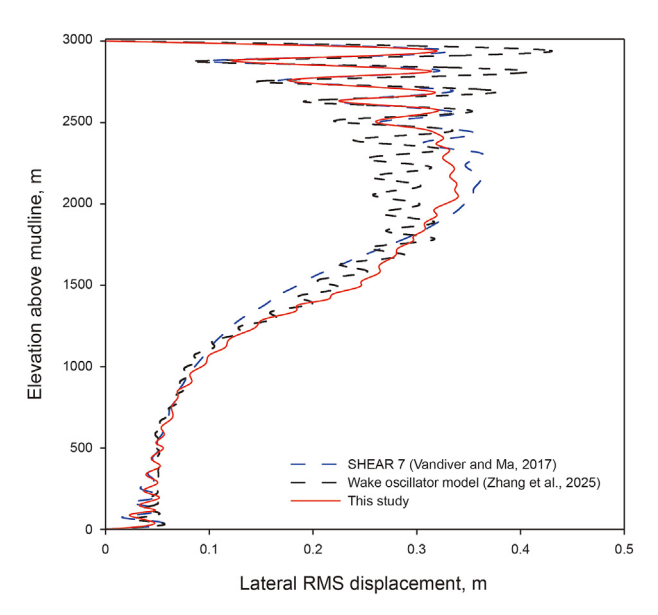


Fig. 16. Model validation results.

2P mode and the vibration frequency will increase with riser outer diameter. However, the riser vibration amplitude shows negative correlation with the outer diameter.

4.2. Simulation results and discussion with considering the riser motion

In order to study the influence of riser motion on VIV, this study conducted parameter sensitivity analysis considering riser motion. Before this, the correctness of the model has been verified firstly. The mechanical model and governing equation of VIV considering riser motion is shown in Appendix E.

4.2.1. Model validation

According the calculation parameters shown in Table 3, the riser RMS displacement obtained by the model established in this paper is compared with previous studies (Vandiver and Ma, 2017; Zhang et al., 2025). The verification result is presented in Fig. 16, which presents that the results of the model in this paper is in good agreement with the analysis results calculated by previous studies. Thus, the model validation is completed.

As can be seen from Fig. 16, the riser RMS displacement is large near the sea surface. As the water depth increases, both the current

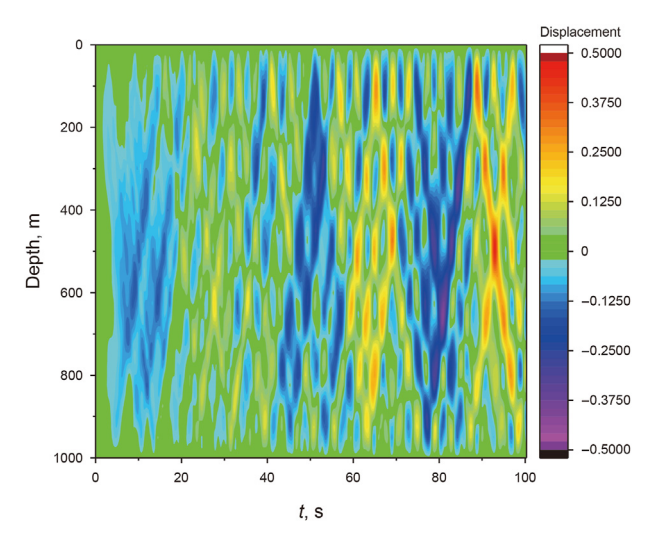


Fig. 17. The transverse VIV of the riser.

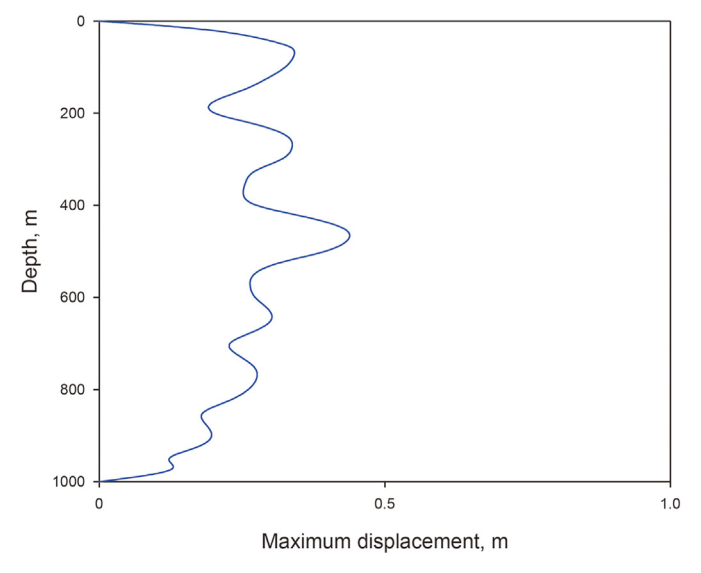


Fig. 18. The maximum transverse VIV displacement of the riser.

Table 4 Parameters used in the simulation.

Parameter	Value	Parameter	Value
Water depth, m	1000	Riser outer diameter, mm	533.4
Steel density, kg/m ³	7850	Riser wall thickness, mm	15.875
Current velocity (at sea surface), m/s	1.2	Current velocity (at seabed), m/s	0.4
Elasticity modulus, GPa	210		

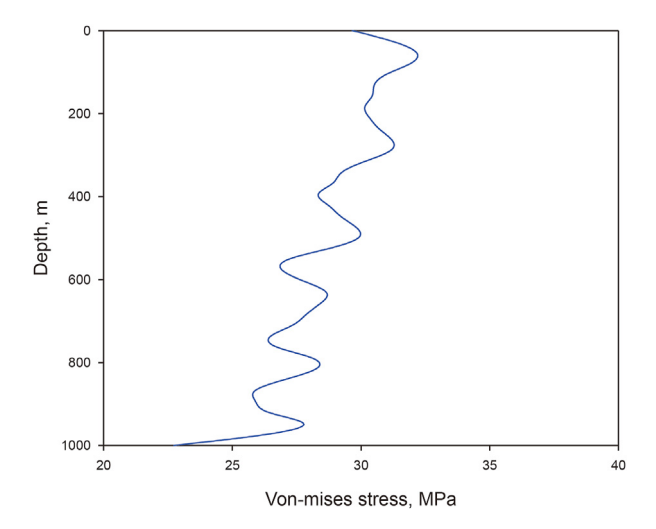


Fig. 19. The maximum von-Mises stress distribution of the riser.

velocity and the riser RMS displacement gradually decrease. The RMS displacement along the length direction of the riser presents the form of standing wave.

4.2.2. Case study

Taking an actual configuration of deepwater drilling riser as example, the current velocity at sea surface is 1.2 m/s and that at seabed is 0.4 m/s. The current velocity change linearly along the water depth. The specific parameters used in simulation are shown in Table 4.

In this study, the slice method is used to simulate the VIV characteristics of riser, where, the riser is divided into 40 units with 25 m per segment. The calculated lateral VIV displacement and von-Mises stress distribution of deepwater drilling riser are shown in Figs. 17—19 respectively.

Fig. 17 shows the transverse VIV displacement cloud map of deepwater drilling riser. As shown in Fig. 17, the vibration mode of the riser changes with time and the transition phenomenon between modes is traveling wave. Fig. 18 shows the distribution of the maximum transverse VIV displacement of deepwater drilling riser. As shown in Fig. 18, the amplitude of vibration displacement increases and then decreases with the increase of water depth. The maximum vibration displacement is 0.256 m which occurs at the depth of 475 m. Fig. 19 shows the distribution of the maximum von-Mises stress of the riser. As shown in Fig. 19, the von-Mises stress distribution of the riser shows downward trend as water depth increases and the maximum von-Mises stress is 32.5 MPa which appears at the depth of 89 m.

The wake vortex shape, dimensionless displacement, lift coefficient and drag coefficient are shown in Figs. 20 and 21, in which the hydrodynamic profile at the water depth of 475 m is extracted.

As shown in Fig. 20, the vortex shedding at water depth of 475 m presents the 2S mode and then changes to the P+S mode gradually. As shown in Fig. 21, the average resistance coefficient of the riser is 0.76, the lift coefficient and displacement fluctuate up and down around 0, and the vortex shedding starts at 6 s.

4.2.3. Parameter sensitivity analysis

(1) Top tension

The transverse VIV displacement, maximum displacement and maximum von-Mises stress are shown in Figs. 22—24 when the top tension of the riser is 1G, 1.25G, 1.5G, 1.75G and 2G, where G is

gravity of the riser in water.

Fig. 22 shows the transverse VIV displacement cloud map of deepwater drilling riser under different top tensions, which reflects the magnitude of vibration displacement through color changes. As shown in Fig. 22, when the top tension is less than or equal to 1.5G, the riser mainly presents seventh order vibration mode, while the riser mainly presents five order vibration mode when the top tension is greater than 1.5G.

Fig. 23 shows the maximum displacement distribution of transverse VIV of the riser under different top tensions. Fig. 24 shows the maximum von-Mises stress distribution under transverse VIV of riser under different top tensions.

As shown in Fig. 23, with the increase of top tension, the maximum displacement of lateral vibration of the riser gradually decreases. When the top tension is 1G, the riser vibration displacement reaches the maximum, which is significantly higher than the other four top tension values. With the increase of the top tension, the riser vibration displacement gradually decreases. However, the variation is relatively small. As shown in Fig. 24, the maximum von-Mises stress of the riser gradually increases with the increase of the top tension. On the whole, considering the VIV characteristics and the equipment capability of floating platform, the top tension is recommended at 1.25G.

(2) Riser wall thickness

The maximum transverse VIV displacement and maximum von-Mises stress distribution are shown in Figs. 25 and 26 when the wall thickness of riser is 0.625, 0.875, 0.9375 and 1.0 in, respectively.

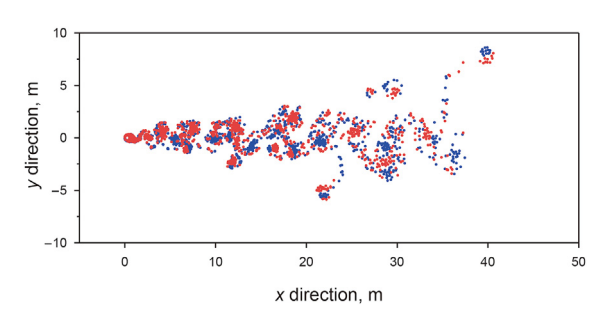


Fig. 20. Vortices distribution of wake field at water depth of 475 m.

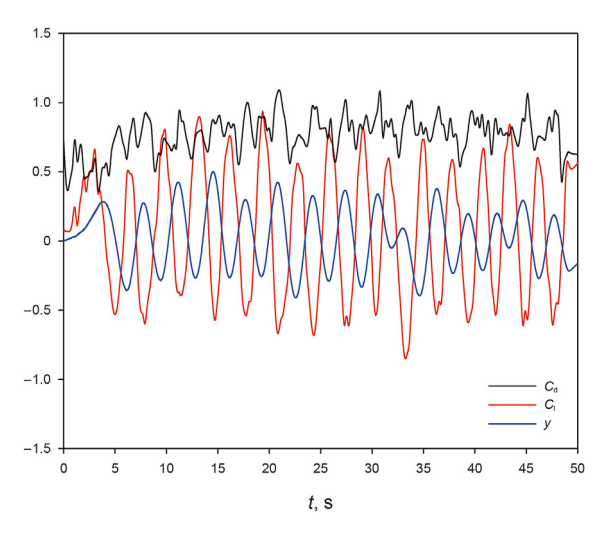
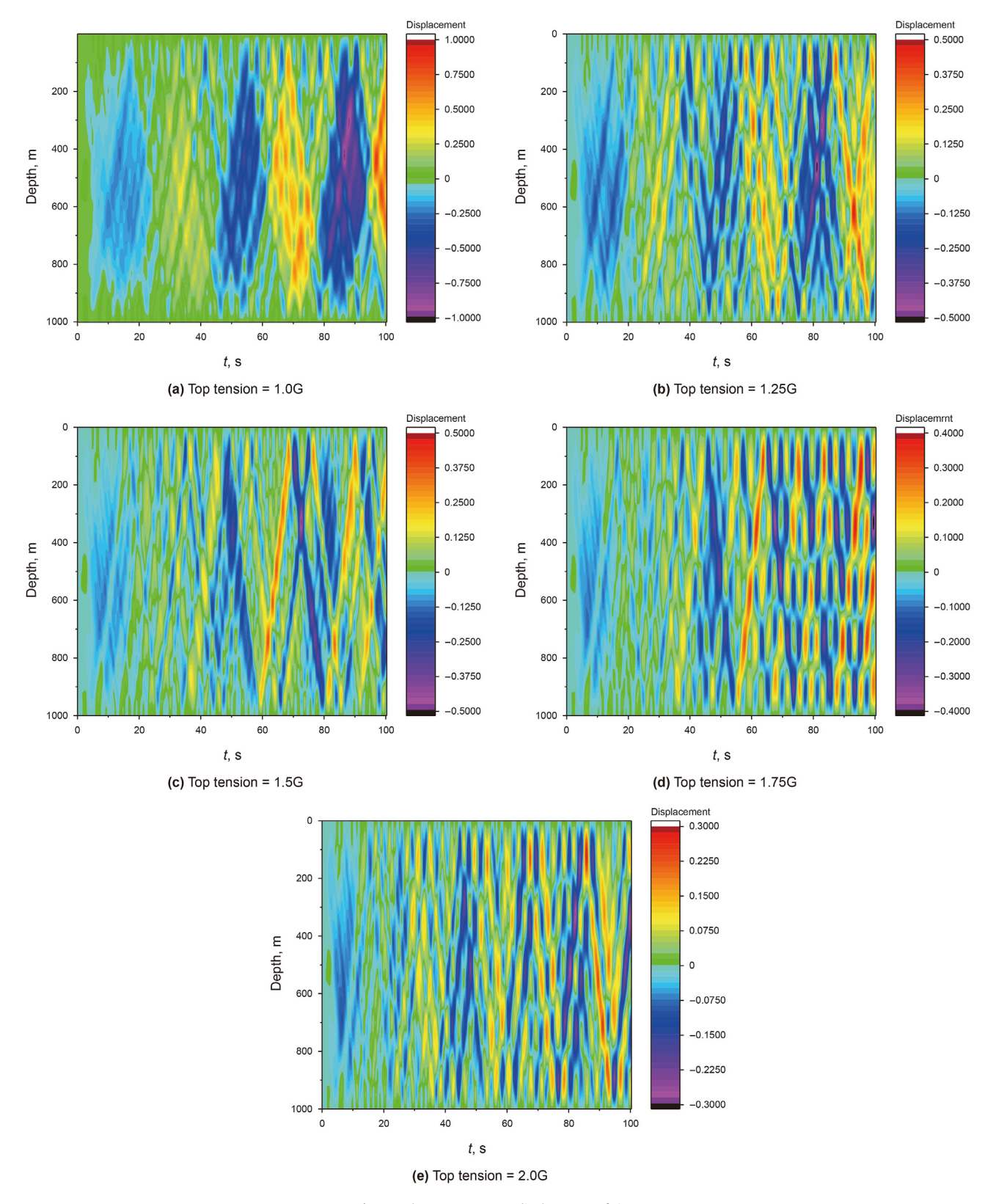


Fig. 21. Dimensionless displacement, lift coefficient and drag coefficient of the riser at water depth of 475~m.



 $\textbf{Fig. 22.} \ \ \textbf{The transverse VIV displacement of riser.}$

As shown in Figs. 25 and 26, with the increase of riser wall thickness, both the maximum lateral displacement and the maximum von-Mises stress gradually decrease. When the wall thickness is 0.625 in, the maximum lateral displacement of

vibration and maximum von-Mises stress is significantly higher than the other three cases. From this perspective, the riser wall thickness should be bigger than 0.875 in.

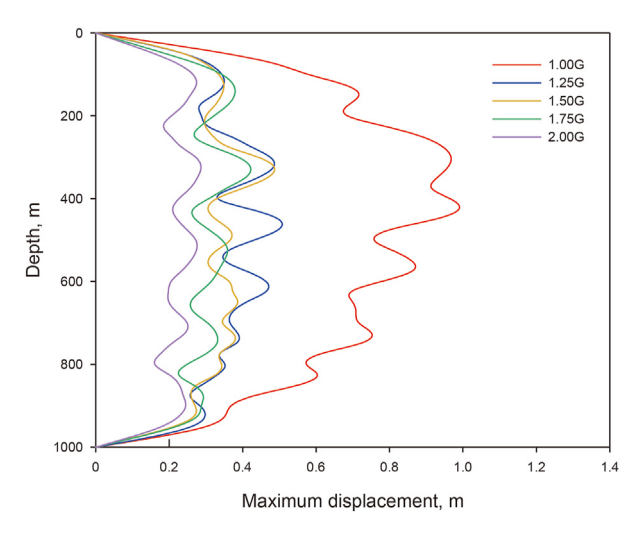


Fig. 23. The maximum transverse VIV displacement of the riser under different top

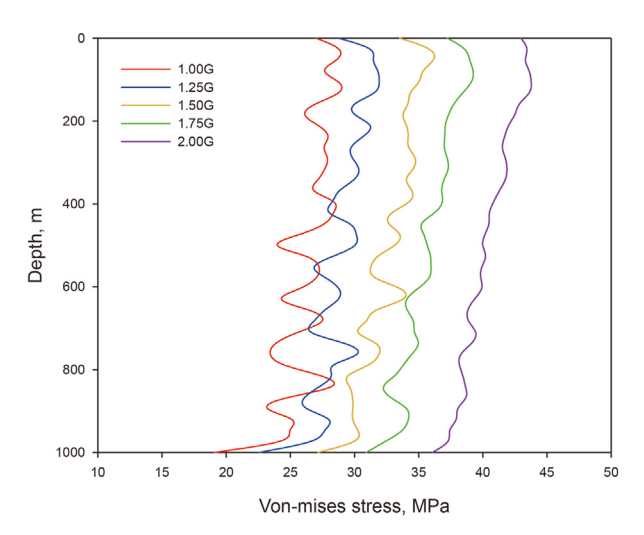


Fig. 24. The maximum von-Mises stress of the riser under different top tension.

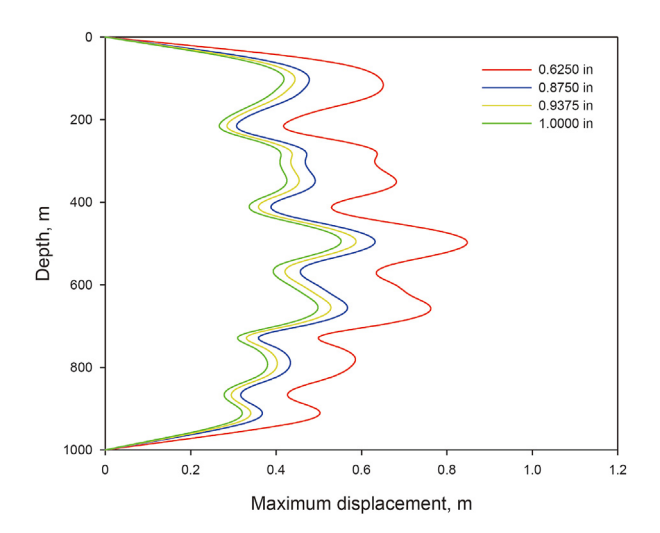


Fig. 25. The maximum transverse VIV displacement of the riser with different wall thickness.

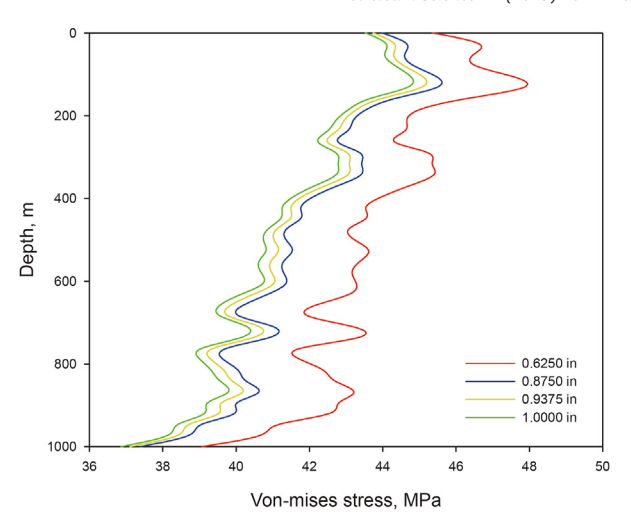


Fig. 26. The maximum von-Mises stress of the riser with different wall thickness.

5. Conclusions

- (1) A numerical model for VIV of deepwater drilling riser has been established based on the DVM and the slice method with consideration of riser motion. In addition, the model validation has also been proved which indicates that the model and method proposed in this study can be used in analysis of VIV of deepwater drilling riser with high accuracy and good engineering application meaning.
- (2) With the increase of flow velocity, the vibration displacement significantly increases. However, the vibration frequency basically remains unchanged. With the increase of outer diameter, the vibration displacement amplitude significantly increased, while the vibration frequency gradually decreases. As the top tension increases, the vibration displacement of the riser gradually decreases. From the aspect of VIV suppression of riser, the top tension is recommended at 1.25G.
- (3) Although the riser motion is considered in this study, the influence of auxiliary lines, supporting structures, different boundary conditions in accordance with actual situation and other factors on the VIV behavior has not been taken into account. Besides, the DVM model still faces challenges in simulating high-density vortices, and future work is also needed to improve model accuracy further.

CRediT authorship contribution statement

Yan-Bin Wang: Writing — review & editing, Writing — original draft, Funding acquisition, Formal analysis, Data curation, Conceptualization. **Hong-Chuan Zhao:** Validation, Methodology. **De-Li Gao:** Supervision. **Rui Li:** Data curation.

Declaration of competing interest

The authors declare that they have no known competing financial interests or personal relationships that could have appeared to influence the work reported in this paper.

Acknowledgement

The authors gratefully acknowledge the financial support from National Key R&D Program of China (Grant number: 2024YFC2815100), Natural Science Foundation of China (Grant

number: 52322110) and Beijing Nova Program (Grant number: 20230484341).

Appendix A

This appendix shows the procedure for solving Eq. (7).

Generally, two kinds of boundary conditions are mainly used, which are Dirichlet boundary condition and Newman boundary condition. The Dirichlet boundary condition is commonly used to specify the value of the potential function on the surface of an object. In this model, there is no relative sliding between the fluid and the riser, which is:

$$\mathbf{U} \cdot \mathbf{S} = \mathbf{U} \cdot \mathbf{n} = 0 \tag{A-1}$$

The Newman boundary condition is commonly used to specify the pressure gradient or normal velocity gradient on the surface of an object, which can be represented as:

$$\mathbf{U} \cdot \mathbf{n} = 0 \tag{A-2}$$

where, S is the unit tangent vector; n is the unit normal vector.

Eq. (7) is a second-order partial differential equation. Therefore, the sum of any particular solution is also the solution of the equation. In fluid mechanics, there are four fundamental solutions to Laplace's equation, which are:

$$\Phi_{\mathbf{u}} = \mathbf{u}_{\infty} r \cos\theta + \mathbf{v}_{\infty} r \sin\theta \tag{A-3}$$

$$\varphi_{\mathbf{s}} = \frac{Q}{2\pi} \ln r \tag{A-4}$$

$$\varphi_{\rm D} = \frac{Q}{2\pi} \frac{\cos\theta}{r} \tag{A-5}$$

$$\varphi_{\mathbf{v}} = \frac{\Gamma}{2\pi} \theta \tag{A-6}$$

where, \mathbf{u}_{∞} is the inflow velocity, m/s; θ is the attack angle, degree; Q is the strength of velocity source, s⁻¹; Γ is the strength of the vortex element.

Since the Laplace equation solutions conform to the superposition principle, the above four solutions can be arbitrarily combined to deal with complex flows. Generally, the thickness of the boundary layer and the internal velocity gradient are determined by the viscosity of the fluid. If the boundary layer is reduced to an infinitesimal thin layer, it can be replaced by multiple panels with a certain vortex strength, and each panel consists of multiple discrete vortex elements. Then, the riser surface can be replaced by finite number of panels with certain vortex strength.

The velocity potential generated by discrete vortex elements at any point in two-dimensional plane can be derived from the Eq. (A-6), thus:

$$\theta = \arctan\left(\frac{y - y_0}{x - x_0}\right) \tag{A-7}$$

where, (x_0, y_0) is the position of the vortex element; (x, y) is the position of certain point in the two-dimensional plane. If the vortex element strength is positive, it causes clockwise velocity, while it causes counterclockwise velocity if the vortex element strength is negative.

Thus, the fluid velocity in any direction v_s can be calculated by:

$$\mathbf{v}_{\mathbf{S}} = \frac{\partial \varphi}{\partial \mathbf{c}} \tag{A-8}$$

By combining Eq. (A-6) and Eq. (A-8), the induced velocity of discrete vortex elements at a certain point in x and y direction can be obtained, which is:

$$\mathbf{u_v} = \frac{\Gamma}{2\pi} \frac{\mathbf{x} - \mathbf{x_0}}{R^2} \tag{A-9}$$

$$\mathbf{v_v} = \frac{\Gamma}{2\pi} \frac{y - y_0}{R^2} \tag{A-10}$$

$$R = \sqrt{(x - x_0)^2 + (y - y_0)^2}$$
 (A-11)

The total induced velocity generated by the vortex element at any position can be obtained by summing the induced velocity generated by multiple discrete vortex elements at this position. Therefore, the induced velocity of vortex element at a certain point in *x* and *y* direction can obtained, which are:

$$\mathbf{u}_{pl} = \frac{\gamma}{2\pi} \left[\arctan\left(\frac{y}{x - x_2}\right) - \arctan\left(\frac{y}{x - x_1}\right) \right]$$
 (A-12)

$$\mathbf{v}_{pl} = \frac{\gamma}{2\pi} \ln \left(\frac{(x - x_2)^2 + y^2}{(x - x_1)^2 + y^2} \right)$$
 (A-13)

Eqs. (A-12) and (A-13) are given in the local unit coordinate system. It is necessary to convert the coordinates of a certain point in the two-dimensional plane to the local coordinate system through substituting the unit normal vector of Eq. (A-14) and the unit tangential vector of Eq. (A-15) into Eqs. (A-12) and (A-13).

Finally, the velocity is converted back to the global coordinate system calculated by Eqs. (A-14) to (A-17), which are:

$$\widehat{\boldsymbol{n}} = (\boldsymbol{n}_{\boldsymbol{X}}, \boldsymbol{n}_{\boldsymbol{V}}) \tag{A-14}$$

$$\widehat{\mathbf{t}} = (\mathbf{t}_{x}, \mathbf{t}_{y}) \tag{A-15}$$

$$\mathbf{u}_{p} = \mathbf{u}_{pl} \cdot \mathbf{t}_{x} + \mathbf{v}_{pl} \cdot \mathbf{n}_{x} \tag{A-16}$$

$$\boldsymbol{v}_p = \boldsymbol{u}_{pl} \cdot \boldsymbol{t}_z + \boldsymbol{v}_{pl} \cdot \boldsymbol{n}_z \tag{A-17}$$

where, \mathbf{u}_p and \mathbf{v}_p are induced velocity components of vortex elements in global coordinate; $\hat{\mathbf{n}}$ is the unit normal vector; $\hat{\mathbf{t}}$ is the unit tangential vector.

Appendix B

This appendix shows the derivation and calculation of vortex strength.

The Dirichlet boundary condition is chosen in this paper. The velocity of each panel is composed of the inflow velocity and the induced velocity of all panels, which is:

$$\mathbf{v}_i = \mathbf{v}_{\infty} + \sum_{i=1}^{N} \mathbf{v}_{ij}^p \tag{B-1}$$

where, v_i is the velocity of vortex plane element.

According to the Dirichlet boundary condition, the tangential velocity at each panel is zero, which is:

$$\mathbf{v}_{\infty} \cdot + \sum_{i=1}^{N} \mathbf{v}_{ij}^{p} \cdot \widehat{\mathbf{t}}_{i} = 0$$
 (B-2)

where, $\mathbf{v}_{ii}^p = (\mathbf{u}_p, \mathbf{v}_p)$ is the velocity generated by vortex plane element i at panel i.

As shown in Eqs. (A-12) and (A-13), the induced velocity of each panel consists of the strength γ_i of the panel j, so Eqs. (A-12) and (A-13) can be written as:

$$\mathbf{u}_{\mathrm{pl}} = \widetilde{\mathbf{u}_{\mathrm{pl}}} \cdot \gamma \tag{B-3}$$

$$\mathbf{v}_{pl} = \widetilde{\mathbf{v}_{pl}} \cdot \gamma$$
 (B-4)

where,
$$\widetilde{\boldsymbol{u}_{pl}} = \frac{1}{2\pi} \left[\arctan \left(\frac{\boldsymbol{y}}{\boldsymbol{x} - \boldsymbol{x}_2} \right) - \arctan \left(\frac{\boldsymbol{y}}{\boldsymbol{x} - \boldsymbol{x}_1} \right) \right]; \qquad \widetilde{\boldsymbol{v}_{pl}} = \frac{1}{2\pi} \ln \left(\frac{(\boldsymbol{x} - \boldsymbol{x}_2)^2 + \boldsymbol{y}^2}{(\boldsymbol{x} - \boldsymbol{x}_1)^2 + \boldsymbol{y}^2} \right).$$
 Eq. (B-2) can be written as:

$$\sum_{i=1}^{N} \left(\widetilde{\boldsymbol{u}_{pl}} \cdot \boldsymbol{t}_{ix} + \widetilde{\boldsymbol{v}_{pl}} \cdot \boldsymbol{t}_{iy} \right) \cdot \gamma_{j} = - \left(\boldsymbol{v}_{\infty x} \cdot \boldsymbol{t}_{ix} + \boldsymbol{v}_{\infty y} \cdot \boldsymbol{t}_{iy} \right)$$
(B-5)

Let $K_{ii}^t = \widetilde{\mathbf{u}_{pl}} \cdot \mathbf{t}_{ix} + \widetilde{\mathbf{v}_{pl}} \cdot \mathbf{t}_{iy}$ be the tangential influence coefficient, which presents the influence of the strength of panel *j* on the tangential velocity at the panel i.

Therefore, Eq. (B-5) can be simplified as:

$$\sum_{j=1}^{N} K_{ij}^{t} \cdot \gamma_{j} = -(\boldsymbol{v}_{\infty X} \cdot \boldsymbol{t}_{iX} + \boldsymbol{v}_{\infty y} \cdot \boldsymbol{t}_{iy})$$
(B-6)

Let $RHS_i = -(\mathbf{v}_{\infty x} \cdot \mathbf{t}_{ix} + \mathbf{v}_{\infty y} \cdot \mathbf{t}_{iy})$, then Eq. (B-6) can be written

$$\sum_{i=1}^{N} K_{ij}^{t} \cdot \gamma_{j} = RHS_{i}$$
 (B-7)

 K_{ii}^{t} and RHS_{i} are only depended on the geometry of the riser and the inflow velocity. If the riser geometry and inflow velocity are given, only γ_i in Eq. (B-7) is unknown. Then, a set of linear equa-

$$\begin{bmatrix} K_{11}^{t} & K_{12}^{t} & K_{13}^{t} & \cdots & K_{1N}^{t} \\ K_{21}^{t} & K_{22}^{t} & K_{23}^{t} & \cdots & K_{2N}^{t} \\ K_{31}^{t} & K_{32}^{t} & K_{33}^{t} & \cdots & K_{3N}^{t} \\ \cdots & \cdots & \cdots & \cdots & \cdots \\ K_{N1}^{t} & K_{N2}^{t} & K_{N3}^{t} & \cdots & K_{NN}^{t} \end{bmatrix} \begin{bmatrix} \gamma_{1} \\ \gamma_{2} \\ \gamma_{3} \\ \vdots \\ \gamma_{N} \end{bmatrix} = \begin{bmatrix} RHS_{1} \\ RHS_{2} \\ RHS_{3} \\ \vdots \\ RHS_{N} \end{bmatrix}$$
(B-8)

Therefore, the vortex strength of each panel can be obtained by solving Eq. (B-9), which is:

$$\gamma = \left(K^{t}\right)^{-1} \cdot RHS \tag{B-9}$$

Appendix C

This appendix shows the derivation of Eq. (12).

The sum of vorticity generated by vortex element at each vortex plane element should be zero, which is:

$$\Gamma_j = \gamma_j \sum_{i=1}^N K_{ij} \Delta S_i = 0 \tag{C-1}$$

Since the total vorticity in non-viscous and incompressible fluid remains constant, the vorticity of vortex plane element can be written as:

$$\Delta\Gamma_i = \gamma_i \cdot \Delta S_i \tag{C-2}$$

Thus, the vorticity sum of the vortex plane element is:

$$\sum_{i=1}^{N} \Delta \Gamma_j = \sum_{i=1}^{N} \gamma_j \cdot \Delta S_j = 0$$
 (C-3)

Substituting Eq. (C-3) into Eq. (B-6), one obtains:

$$\sum_{j=1}^{N} \left(K_{ij}^{t} + \Delta S_{j} \right) \cdot \gamma_{j} = - \left(\boldsymbol{v}_{\infty X} \cdot \boldsymbol{t}_{iX} + \boldsymbol{v}_{\infty y} \cdot \boldsymbol{t}_{iy} \right)$$
 (C-4)

If considering the influence of free vortices, one obtains:

$$\sum_{i=1}^{N} \left(K_{ij}^{t} + \Delta S_{j} \right) \cdot \gamma_{j} = -\left(\boldsymbol{v}_{\infty X} \cdot \boldsymbol{t}_{ix} + \boldsymbol{v}_{\infty y} \cdot \boldsymbol{t}_{iy} \right) - \sum_{k=1}^{N_{y}} \Delta \Gamma_{k} \left(\widetilde{\boldsymbol{u}_{ik}} \cdot \boldsymbol{t}_{ix} + \widetilde{\boldsymbol{v}_{ik}} \cdot \boldsymbol{t}_{iy} \right)$$
(C-5)

tions of order N can be obtained, which is:

Then, Eq. (12) can be obtained considering that the sum of vorticity generated by each vortex element at each vortex plane element is zero.

Appendix D

This appendix shows the derivation of Eqs. (26) and (27).

The force on the riser can be obtained by the integration of the pressure on the surface, and the pressure can be obtained by the vorticity change on the surface of the riser when the convection and diffusion of vortices are completed. Under this circumstance, the N-S equation can be simplified as:

$$-\frac{1}{\rho}\nabla p = \frac{\partial \mathbf{v}}{\partial t} \tag{D-1}$$

If velocity is expressed in terms of surface vorticity, the Eq. (D-1) can be written as:

$$\frac{1}{\rho} \frac{\partial p}{\partial s} = -\frac{\partial \gamma(s)}{\partial t} \tag{D-2}$$

For a certain discrete vortex element, the surface pressure variation in each time step is:

$$\Delta p_i = -\rho \frac{\Delta \Gamma_i}{\Delta t} \tag{D-3}$$

The surface pressure of certain panel can be obtained by integration of Eq. (D-3), which is:

$$P_i = P_1 - \frac{\rho}{\Delta t} \sum_{j=1}^i \Delta \Gamma_j \tag{D-4}$$

where, P_1 is the pressure at the reference point; $\Delta \Gamma_j$ is the variation of vorticity of any vortex plane element.

$$p_i = -\frac{\rho}{\Delta t} \Delta \Gamma_i^{\rm S} \tag{D-5}$$

Let Δp be the difference between p_{max} and the pressure at the former stagnation point, one obtains:

$$\Delta p = p_{\infty} + \frac{1}{2} \rho_{\infty} \mathbf{v}_{\infty}^2 - p_{\text{max}} = p_{\infty} + \frac{1}{2} \rho_{\infty} \mathbf{v}_{\infty}^2 + \frac{\rho}{\Delta t} \Delta \Gamma_{\text{max}}^{\text{s}}$$
 (D-6)

Then, the surface pressure of any vortex element can be expressed as the relative pressure to the former stagnation point, which is:

$$p_{i} = \Delta p - \frac{\rho}{\Delta t} \Delta \Gamma_{i}^{s} = p_{\infty} + \frac{1}{2} \rho_{\infty} \mathbf{v}_{\infty}^{2} - \frac{\rho}{\Delta t} \left(\Delta \Gamma_{i}^{s} - \Delta \Gamma_{\max}^{s} \right)$$
(D-7)

The pressure coefficient can be expressed as:

$$cp_i = \frac{p_i - p_{\infty}}{0.5p_{\infty} \mathbf{v}_{\infty}^2} = 1 - \frac{2}{\mathbf{v}_{\infty}^2 \Delta t} \left(\Delta \Gamma_i^s - \Delta \Gamma_{\text{max}}^s \right)$$
 (D-8)

If the pressure coefficient on the surface of the riser is obtained, the horizontal and vertical force coefficient can be obtained by integrating the pressure coefficient along the surface of the riser, which are:

$$CF_{x} = -\frac{1}{c} \sum_{i=1}^{N} c p_{i} n_{ix} \Delta S_{i}$$
 (D-9)

$$CF_{y} = -\frac{1}{c} \sum_{i=1}^{N} c p_{i} n_{iy} \Delta S_{i}$$
 (D-10)

Appendix E

This appendix shows the mechanical model and solution procedure of VIV considering riser motion.

The mechanical model of the VIV of deepwater drilling riser is shown in Fig. E-1. The top of the riser is connected to the floating drilling platform, and the bottom is connected to the subsea well-head

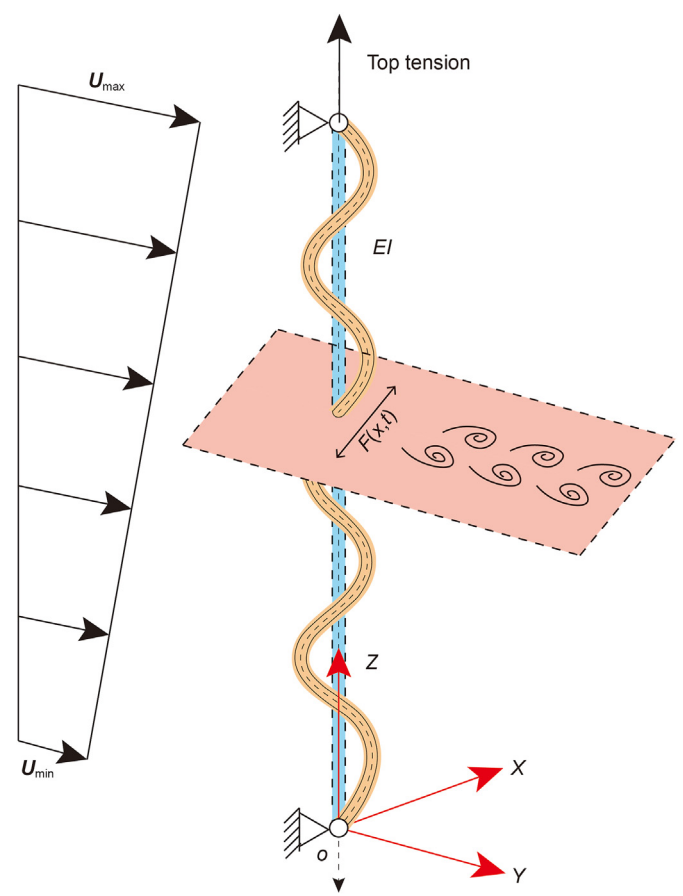


Fig. E-1 Schematic diagram of mechanical model of VIV of deepwater drilling riser.

The governing equation and boundary conditions describing VIV can be written as:

$$EI\frac{\partial^4 y}{\partial x^4} - T(x)\frac{\partial^2 y}{\partial x^2} + m\frac{\partial^2 y}{\partial t^2} = f(x, t)$$
 (E-1)

In this paper, both the top and the bottom of the riser are regarded as fixed ends. Then, the boundary conditions can be written as:

$$\begin{cases} y(x)|_{x=0} = 0, \frac{\partial^2 y}{\partial x^2}|_{x=0} = 0\\ y(x)|_{x=l} = 0, \frac{\partial^2 y}{\partial x^2}|_{x=l} = 0 \end{cases}$$
(E-2)

The initial conditions are:

$$\begin{cases} y(t)|_{t=0}=0\\ \frac{\partial y}{\partial t}|_{t=0}=0 \end{cases} \tag{E-3}$$

where, y is the transverse VIV displacement of the riser, m; T(x) is the axial tension force, N; m is the mass per unit length of the riser, kg/m; f(x,t) is the lift force caused by inflow, N.

$$f(x,t) = \frac{1}{2}\rho v^2 SC_I \tag{E-4}$$

where, S is the projective area per unit length which is equal to the diameter of the riser, m; C_I is the lift coefficient.

In this paper, finite difference method and fourth-order Runge-Kutta method are used to solve the governing equation.

Eq. (E-1) can be written as:

$$\frac{\partial^2 y}{\partial t^2} = -\frac{EI}{m} \frac{\partial^4 y}{\partial x^4} + \frac{T}{m} \frac{\partial^2 y}{\partial x^2} + \frac{1}{m} f(x, t)$$
 (E-5)

Let $(t) = \frac{\partial y}{\partial t}$, then:

$$\frac{\partial}{\partial t} \begin{pmatrix} y \\ v \end{pmatrix} = \begin{pmatrix} -\frac{EI}{m} \frac{\partial^4 y}{\partial x^4} + \frac{T}{m} \frac{\partial^2 y}{\partial x^2} + \frac{1}{m} f(x, t) \end{pmatrix}$$
 (E-6)

The difference form of Eq. (E-6) can be expressed as:

$$A = \begin{bmatrix} -2 & 1 & 0 & 0 & \cdots & 0 & 0 & 0 \\ 1 & -2 & 1 & 0 & \cdots & 0 & 0 & 0 \\ 0 & 1 & -2 & 1 & \cdots & 0 & 0 & 0 \\ \vdots & \vdots & \vdots & \vdots & \ddots & \vdots & \vdots & \vdots \\ 0 & 0 & 0 & 0 & \cdots & -2 & 1 & 0 \\ 0 & 0 & 0 & 0 & \cdots & 1 & -2 & 1 \\ 0 & 0 & 0 & 0 & \cdots & 0 & 1 & -2 \end{bmatrix}$$

The vector form of Eq. (E-8) is

(E-5)
$$\begin{cases} y_{k+1} = y_k + v_k \cdot dt \\ v_{k+1} = v_k + \left(-\frac{EI}{m} \frac{B \cdot y_k}{h^4} + \frac{T}{m} \frac{A \cdot y_k}{h^2} + \frac{1}{m} f(x, t) \right) \cdot dt \end{cases}$$
 (E-9)

The fourth-order Runge-Kutta method can be written as:

$$y_{n+1} = y_n + \frac{h}{6}(k_1 + 2k_2 + 2k_3 + k_4)$$
 (E-10)

$$\frac{\partial}{\partial t} \begin{pmatrix} y \\ v \end{pmatrix} = \begin{pmatrix} -\frac{EI}{m} \frac{y_{k+2} - 4y_{k+1} + 6y_k - 4y_{k-2} + y_{k-2}}{h^4} + \frac{T}{m} \frac{y_{k+1} - 2y_k + y_{k-1}}{h^2} + \frac{1}{m} f(x, t) \end{pmatrix}$$
(E-7)

Eq. (E-7) can be written as:

$$\frac{\partial}{\partial t} \begin{pmatrix} y \\ v \end{pmatrix} = \begin{pmatrix} v \\ -\frac{EI}{m} \frac{\partial^4 y}{\partial x^4} + \frac{T}{m} \frac{\partial^2 y}{\partial x^2} + \frac{1}{m} f(x, t) \end{pmatrix}$$
 (E-8)

where,

$$\begin{cases} k_{1} = f(y_{n}, t_{n}) \\ k_{2} = f\left(y_{n} + \frac{1}{2}k_{1}\Delta t, t_{n} + \frac{1}{2}\Delta t\right) \\ k_{3} = f\left(y_{n} + \frac{1}{2}k_{2}\Delta t, t_{n} + \frac{1}{2}\Delta t\right) \\ k_{4} = f(y_{n} + k_{3}\Delta t, t_{n} + \Delta t) \end{cases}$$
(E-11)

Substituting Eqs. (E-10) and (E-11) into Eq. (E-9), and the VIV displacement of the riser can be obtained by iteration.

References

- Birkhoff, G., Zarantanello, J., 1957. Wakes and Cavities. Academic Press, New York. Bishop, R.E.D., Hassan, A.Y., 1964. The lift and drag forces on a circular cylinder oscillating in a flowing fluid. Proceedings of the Royal Society A 277 (1368), 51–75. https://doi.org/10.1098/rspa.1964.0005.
- Blevins, R.D., 1984. Applied Fluid Dynamics Handbook. Van Nostrand Reinhold Company Reinhold, New York.
- Bourguet, R., Karniadakis, G.E., Triantafyllou, M.S., 2011. Vortex-induced vibrations of a long flexible cylinder in shear flow. J. Fluid Mech. 677, 342–382. https://doi.org/10.1017/ifm.2011.90.
- Chorin, A.J., 1973. Numerical study of slightly viscous flow. J. Fluid Mech. 57 (4), 785–796. https://doi.org/10.1017/S0022112073002016.
- Facchinetti, M.L., Langre, E.D., Biolley, F., 2004. Coupling of structure and wake oscillators in vortex-induced vibrations. J. Fluid Struct. 19 (2), 123–140. https://doi.org/10.1016/j.jfluidstructs.2003.12.004.
- Farshidianfar, A., Zanganeh, H.A., 2010. A modified wake oscillator model for vortex-induced vibration of circular cylinders for a wide range of mass-damping ratio.
 J. Fluid Struct. 26 (3), 430–441. https://doi.org/10.1016/j.jfluidstructs.2009.11.005.
 Feng CC. 1968. The Management CV.
- Feng, C.C., 1968. The Measurement of Vortex Induced Effects in Flow Past Stationary and Oscillating Circular and D-Section Cylinders. University of British Columbia, Canada. https://doi.org/10.14288/1.0104049.
- Griffin, O.M., Steven, E.R., 1976. Vortex shedding from a cylinder vibrating in line with an incident uniform flow. J. Fluid Mech. 75 (2), 257–271. https://doi.org/ 10.1017/S0022112076000207.
- Hartlen, R.T., Currie, I.G., 1970. Lift-oscillator Model of vortex-induced vibration. J. Eng. Mech. 96, 577–591. https://doi.org/10.1061/JMCEA3.0001562.
- Januvtis, N., Williamson, C.H.K., 2003. Vortex-induced vibration of a cylinder with two degrees of freedom. J. Fluid Struct. 17 (7), 1035–1042. https://doi.org/10.1016/S0889-9746(03)00051-3.
- Khalak, A., Williamson, C.H.K., 1999. Motions, forces and mode transitions vortex induced vibrations at low mass-damping. J. Fluid Struct. 13 (7), 813–851. https://doi.org/10.1006/jfls.1999.0236.
- Kumar, P.R., Nallayarasu, S., 2022. VIV response of risers with large aspect ratio and low rigidity using a numerical scheme based on wake oscillator model. Appl. Ocean Res. 118, 103011. https://doi.org/10.1016/j.apor.2021.103011.
- Lewis, R.I., 1991. Vortex Element Methods for Fluid Dynamic Analysis of Engineering Systems. Cambridge University Press. https://doi.org/10.1017/CB09780511529542.001.

- Li, X.H., Yuan, Y.C., Duan, Z.D., et al., 2023. Coupling effect of time-varying axial tension and combined unsteady flow on vortex-induced vibration of flexible risers. Ocean Engineering 285, 115358. https://doi.org/10.1016/j.oceaneng.2023.115358.
- Li, M., Deng, D., Wan, D.C., 2021. Numerical simulation of vortex-induced vibration of a flexible riser with attached splitter plate. Chinese Journal of Hydrodynamics 36 (1), 112–120. https://doi.org/10.16076/j.cnki.cjhd.2021.01.015 (in Chinese).
- Lucor, D., Imas, L., Karniadakis, G.E., 2001. Vortex dislocations and force distribution of long flexible cylinders subjected to sheared flows. J. Fluid Struct. 15 (3–4), 641–650. https://doi.org/10.1006/ifls.2000.0366.
- Mao, L.J., Yan, J.X., Zeng, S., et al., 2023. Vortex-induced vibration characteristics of mining riser under the coupling effect of external ocean current and internal multiphase flow. Appl. Ocean Res. 140, 103747. https://doi.org/10.1016/ j.apor.2023.103747.
- Norberg, C., 2003. Fluctuating lift on a circular cylinder: review and new measurements. J. Fluid Struct. 17 (1), 57–96. https://doi.org/10.1016/S0889-9746(02)
- Oertel, J.H., 1990. In: Annual Review of Fluid Mechanics, vol. 22. Annual Reviews Inc., pp. 539–562. https://doi.org/10.1146/annurev.fl.22.010190.002543
- Owen, M., Griffin, O.M., Steven, E.R., 1975. On vortex strength and drag in bluff-body wakes. J. Fluid Mech. 69 (4), 721–728. https://doi.org/10.1017/S0022112075001656.
- Rimmer, J.D.T., 2001. Aerodynamic Flow Simulation Using the Vortex Cloud Method to Predict the Performance of Lifting Bodies. University of Manitoba.
- Tian, Q.L., 2016. Numerical Simulation of Flow and Vortex Induced Vibration of Two Circular Cylinders by Using Discrete Vortex Method. Shanghai Jiao Tong University (in Chinese).
- Vandiver, J.K., Ma, L., 2017. Does more tension reduce VIV? The 36th International Conference on Offshore Mechanics and Arctic Engineering. American Society of Mechanical Engineers. https://doi.org/10.1115/OMAE2017-61435
- Williamson, C.H.K., Roshko, A., 1988. Vortex formation in the wake of an oscillating cylinder. J. Fluid Struct. 2 (4), 355–381. https://doi.org/10.1016/S0889-9746(88) 90058-8.
- Zhang, G.R., Wang, Y.B., Gao, D.L., 2025. Numerical analysis of vortex-induced vibration of deepwater drilling riser based on Van der Pol wake oscillator model. Mar. Struct. 99, 103711. https://doi.org/10.1016/j.marstruc.2024.103711.
- Zhao, P.L., Wang, J.S., Jiang, S.Q., et al., 2010. Numerical simulation of fluid-Structural interaction for vortex-induced vibration of riser. Ocean Technology 29 (3), 73–77 (in Chinese).